INL/JOU-24-81348-Revision-0

Electric field-assisted embedding of fiber optic sensors in structural materials for structural health monitoring

February 2025

Xinchang Zhang, Joshua E Daw, Charles Nelson Payne, Bibo Zhong, Austin D Fleming, Zilong Hua, Jorgen Fredrick Rufner

INL/JOU-24-81348-Revision-0

Electric field-assisted embedding of fiber optic sensors in structural materials for structural health monitoring

Xinchang Zhang, Joshua E Daw, Charles Nelson Payne, Bibo Zhong, Austin D Fleming, Zilong Hua, Jorgen Fredrick Rufner

February 2025

Idaho National Laboratory
Idaho Falls, Idaho 83415

http://www.inl.gov

Prepared for the
U.S. Department of Energy
Under DOE Idaho Operations Office
Contract DE-AC07-05ID14517

Journal of Materials Research and Technology 34 (2025) 15–31

Contents lists available at ScienceDirect

Journal of Materials Research and Technology

journal homepage: www.elsevier.com/locate/jmrt

Electric field-assisted embedding of fiber optic sensors in structural materials for structural health monitoring

Xinchang Zhang *, Joshua Daw, Charles Payne, Bibo Zhong, Austin Fleming, Zilong Hua, Jorgen Rufner

Idaho National Laboratory, Idaho Falls, ID, 83415, United States

ARTICLE INFO

Handling editor: M Meyers

Keywords:
Fiber optic sensor
Embedded sensor
OFDR
High temperature
Health monitoring
Sintering

ABSTRACT

Embedding fiber optic sensors in critical components is a key step for real-time monitoring of structural conditions during service and supporting autonomous system operations. Successful integration of these sensors necessitates effective interfacial bonding between the fiber and matrix, good integrity and functionality of the embedded sensors, robust mechanical strength of the matrix materials, and the ability to retain these properties during transient thermal and stress events. This study demonstrates the encapsulation of fused silica optical fibers in stainless steel and nickel through the electric field-assisted sintering (EFAS) process. Copper-coated and gold-coated single mode optical fibers were embedded under different EFAS conditions. The resulting components with embedded sensors were evaluated using advanced microscopy and optical frequency domain reflectometry (OFDR) to assess the aforementioned critical aspects of embedding. The results indicate that both copper- and gold-coated fibers can be successfully embedded in stainless steel and nickel with good fiber integrity and fiber-matrix bonding. Samples fabricated under optimal conditions passed helium leak testing, confirming effective interfacial bonding. Microstructural characterization revealed excellent fiber-matrix adhesion and interdiffusion of elements across the interface. The functionality of the embedded fibers was evaluated through OFDR scans, which revealed signal insertion loss of 0.43–0.52 dB for nickel samples and 0–0.75 dB for stainless steel samples at the embedding sites. Additionally, the embedded fibers underwent cyclic thermal treatment between 500 °C and 700 °C. The fibers maintained good integrity and interfacial characteristics, demonstrating their ability to survive cyclic thermal events for sensing in harsh environments.

1. Introduction

Structural health monitoring (SHM) has garnered substantial attention over the past few decades across various industries as a predictive tool for assessing degradation and damage in structures and materials over time [1]. SHM involves the continuous collection of precise, real-time data of variables during a component's service life. This systematic monitoring delivers essential information for evaluating structural health, enabling timely maintenance decisions to ensure system safety, performance, and longevity. In-service monitoring of structural performance has played a significant role not only in critical civil and geotechnical infrastructures [2], but also in aerospace and energy systems, such as jet engines [3], wind turbines [4], and nuclear reactors [5]. The growing importance of SHM in modern advanced systems is of particular interest because these systems are designed to operate in more extreme environments to boost performance and efficiency, which in turn poses unprecedented loads on the components. To implement SHM, a key element is data acquisition through sensor network that can provide real-time sensing data for structure condition assessment.

Fiber optic sensors have emerged as a breakthrough technology in SHM. These sensors exploit the unique properties of optical fibers to measure a wide range of physical parameters, such as strain, temperature, vibration, humidity, acceleration, and irradiation, with remarkable accuracy and sensitivity. Fiber optic sensors typically employ Fiber Bragg Grating (FBG) or distributed sensing techniques, enabling the measurement of both localized and distributed data along the length of a fiber with a high spatial resolution [6]. This addresses the limitations of conventional strain gauges and thermocouples, which are often restricted to single-point measurements. Moreover, fiber optic sensors offer high sensitivity and accuracy, immunity to electromagnetic interference, multiplex sensing capability, reliable performance in harsh environments, and lightweight and flexibility [7]. These unique

* Corresponding author.
E-mail address: xinchang.zhang@inl.gov (X. Zhang).

https://doi.org/10.1016/j.jmrt.2024.12.050
Received 23 October 2024; Received in revised form 25 November 2024; Accepted 4 December 2024
Available online 5 December 2024

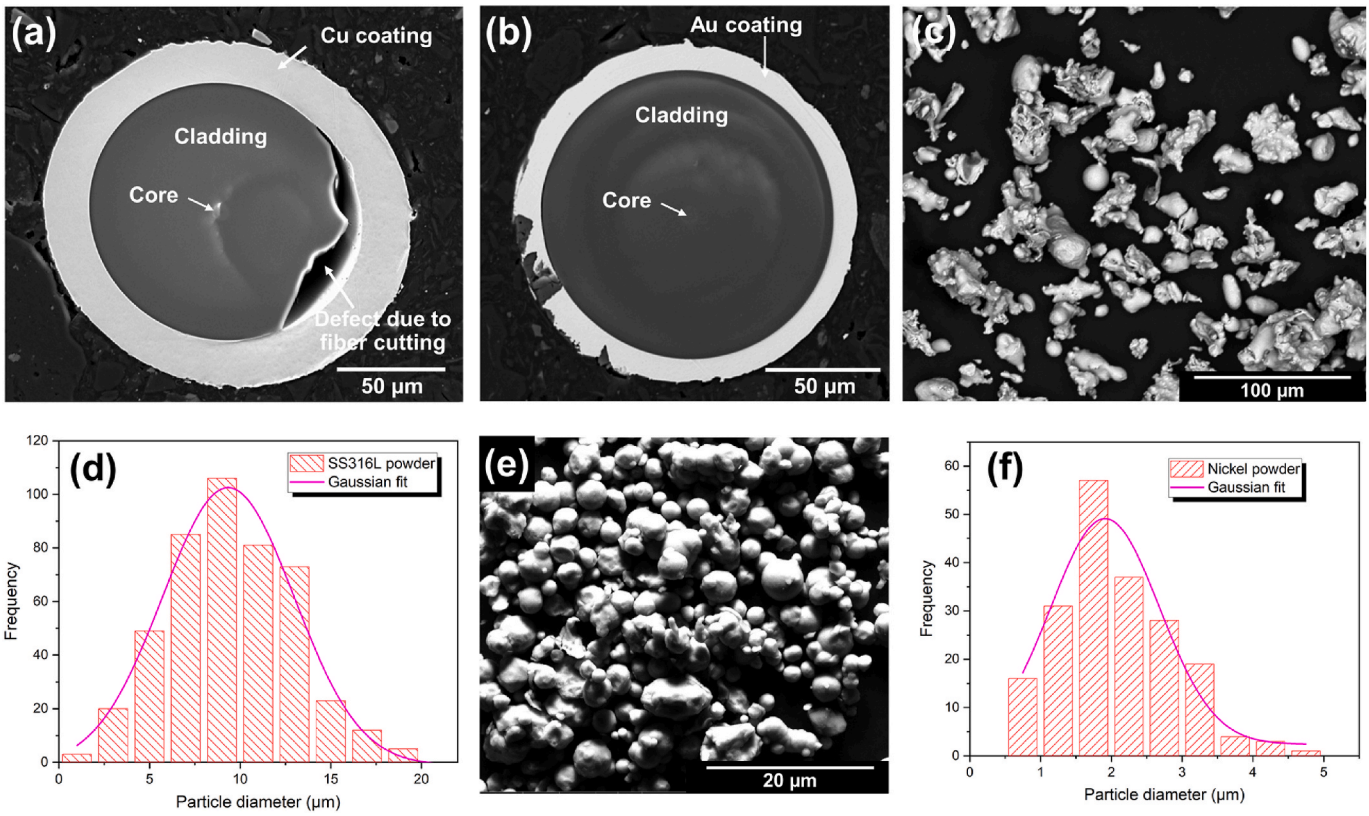

Fig. 1. SEM cross-sectional images of the as-received (a) Cu-coated and (b) Au-coated fibers. SEM micrographs showing the particle morphology of (c) SS powder and (e) nickel powder. Particle size distribution for (d) SS and (f) nickel powder.

Table 1
Specifications of as-received Cu-coated and Au-coated fibers.

Property	Fiber type	
	Cu-coated	Au-coated
Fiber diameter	165 μm (coating) 125 μm (cladding) 9 μm (core)	155 μm (coating) 125 μm (cladding) 9 μm (core)
Coating materials	Copper alloy	Gold
Coating thickness	20 ± 5 μm	15 ± 5 μm
Melting point (coating)	~1085 °C	~1064 °C
Wavelength	1300–1600 nm	633–680 nm
Preform	Ge-doped core	Ge-doped core
Tensile strength	689.5 MPa	3.3 GPa
Attenuation	9.5 dB/km	4 dB/Km
Operation temperature	<600 °C	<700 °C

Table 2
Chemical composition of the SS316L powder.

Element	Fe	Ni	Cr	Mo	Mn	Si	C	P	S
Wt. %	Bal.	12	17	2.5	2	0.75	0.03	0.045	0.03

advantages have led to their widespread adoption in various fields. For instance, fiber optic sensors were embedded in lithium-ion batteries to monitor internal strain and temperature for battery life cycle management [8]. Monitoring of temperature and strain in a microreactor heat pipe was realized with embedded fiber optic sensors [9]. Furthermore, fiber optic sensors have been employed to detect bonding issues in aircraft wing structures [10]. In addition, these sensors have been used in the healthcare industry to continuously measure abdominal and thoracic respiratory movement under medical imaging [11].

Embedding fiber optic sensors within parts of interest is a key step for SHM because it enables real-time monitoring of internal and distributed data, enhances sensing accuracy and sensitivity (e.g., fiber-matrix temperature and strain coupling), benefits structure compactness, and enables the shielding from external environmental influences (e.g., corrosive media) that may affect sensor durability [12]. Previous endeavors have employed several techniques to encapsulate fiber optic sensors in metallic and ceramic materials, mainly using additive manufacturing (AM) techniques such as ultrasonic AM (UAM) [9, 13–22], directed energy deposition (DED) [23–25], powder bed fusion (PBF) [26–28], and binder jetting (BJ) [29].

UAM is a solid-state additive process that bonds layered metal foils through plastic deformation of materials at mating surfaces induced by applied pressure and vibration [22]. UAM is particularly advantageous for fiber embedding due to its low processing temperature (~170 °C for aluminum and copper alloys [21]), which minimizes the risk of fiber breakage. For instance, Zhao et al. [21] utilized UAM to embed FBGs in Al-6061 and showcased dynamic strain measurements. Chilelli et al. [20] demonstrated the detection of crack initiation and propagation with FBGs embedded into Al-6061 obtained by UAM. He et al. [19] implanted a single-mode fiber sensor in Al-1100 and revealed strain response under tensile loading. The use of UAM for embedding fiber optic sensors has also been reported in other studies [9,15–18]. UAM has shown success in embedding fibers within low-strength materials, such as aluminum and copper alloys, where effective bonding between the fiber and matrix can be achieved. Notable examples include metallized fibers (aluminum-coated and copper-coated) encapsulated in Al-3003 matrix via UAM, which exhibited void-free fiber-matrix bonding, although some non-bonded regions were observed at matrix interfaces [14]. Additionally, copper-coated fibers integrated into Al-6061 possessed good bonding under optimal processing conditions [13]. However, UAM faces significant challenges when joining high-strength materials, such as stainless steel (SS) and nickel-based alloys that are commonly used in high-temperature applications. As a result, fibers

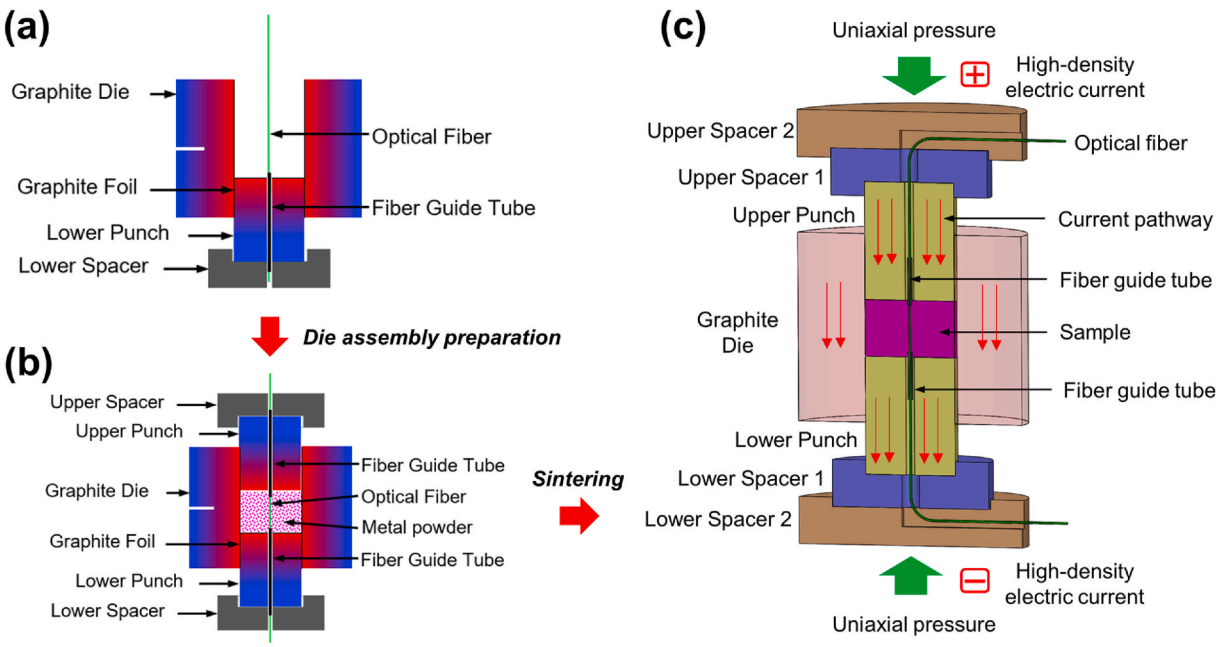

Fig. 2. Schematic representation of the fiber embedding process using EFAS. (a) Vertical placement of a fiber in the die. (b) Die assembly containing metal powder and fiber. (c) 3D sectional view showing the positioning of the fiber within the die assembly.

Table 3
Parametric matrix for consolidating SS316L and nickel with optical fibers and resulting sample relative density.

	Sample ID.	Temperature (°C)	Pressure (MPa)	Hold time (min)	Sample density (%)
Cu-coated fiber embedded in SS316L	CuF-SS-800-40-5	800	40	5	79.3%
	CuF-SS-900-40-5	900	40	5	84.3%
	CuF-SS-980-40-5	980	40	5	92.2%
	CuF-SS-980-50-5	980	50	5	94.1%
	CuF-SS-980-60-10	980	60	10	97.0%
Cu-coated fiber embedded in Ni	CuF–Ni-800-40-5	800	40	5	96.5%
	CuF–Ni-900-50-5	900	50	5	98.8%
	CuF–Ni-980-50-5	980	50	5	98.8%
Au-coated fiber embedded in SS316L	AuF-SS-800-40-5	800	40	5	78.8%
	AuF-SS-900-40-5	900	40	5	84.3%
	AuF-SS-980-40-5	980	40	5	92.1%
	AuF-SS-980-50-5	980	50	5	94.7%

embedded in these materials tend to show poor bonding. For instance, one study reported that optical fibers embedded in SS304 exhibited large voids at fiber-matrix interface and at the interfaces of SS304 layers [9]. It has been widely documented that high-temperature materials joined by UAM often show defects at the interfaces [30–33], which compromise the mechanical properties of the materials.

Laser-based DED and PBF have also been explored for embedding optical fibers. In these processes, optical fibers were placed on substrates or previously deposited layers and subsequently covered with additional material layers processed by a laser beam. A significant challenge with these methods is to protect the fibers from thermal damage. Typically, metal coatings, such as nickel, chromium, or copper, were applied to facilitate fiber embedding [23–28]. Furthermore, a precisely machined groove on the substrate, tailored to the diameters of the coated fibers, is essential for proper fiber placement and protection [25,26]. An inadequately machined groove can result in fiber breakage, while an excessively machined groove may lead to large voids at the joint [25]. Successful embedding with optimal fiber functionality and bonding quality requires careful tuning of processing parameter. However, gaps at the interface below the fiber are difficult to prevent because of the inaccessibility of laser source to this region when it scans on the top of the substrate [24–27,34]. These gaps limit the use of the final component in high-pressure applications where effective sealing is critical. Additionally, these voids can adversely impact component performance and introduce uncertainties in strain and temperature measurements.

To address the aforementioned challenges, this study demonstrates an embedding technique based on electric field-assisted sintering (EFAS). EFAS utilizes electric current to synthesize materials and is capable of processing a diverse array of metallic, ceramic, and composite materials [35]. This study aims to demonstrate successful embedding by investigating several key aspects: 1) process and parameters optimization to achieve optimal overall properties; 2) inspection of fiber integrity and functionality through advanced microscopy and optical property measurements; 3) characterization of fiber-matrix bonding using microscopes and helium leak testing; 4) machinability of parts with embedded sensors; and 5) assessment of fiber integrity and bonding condition after thermal cycling. A systematic investigation of these properties highlights the potential of EFAS technology for integrating fiber optic sensors into high-temperature materials for SHM applications.

2. Research methodology

2.1. Fiber and matrix materials

Fused silica fibers have been demonstrated to operate at temperatures exceeding 800 °C [36]. However, for sensing applications in high-temperature environments (>500 °C), typical polymer-coated fibers are unsuitable, which necessitates the use of metal-coated fibers. In

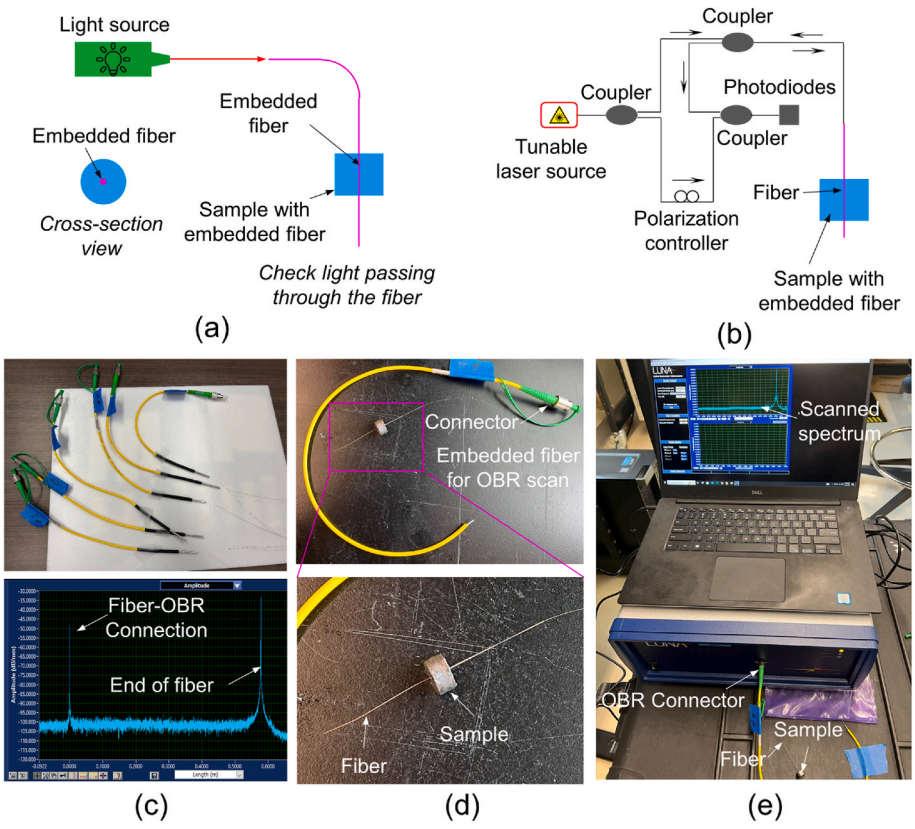

Fig. 3. Optical transmission and OFDR analysis of as-received and encapsulated fibers. Schematics of (a) transmission testing and (b) OFDR technique. (c) Fibers before embedding and Rayleigh scattering pattern. (d) Embedded fiber for OBR scan. (e) OBR test setup.

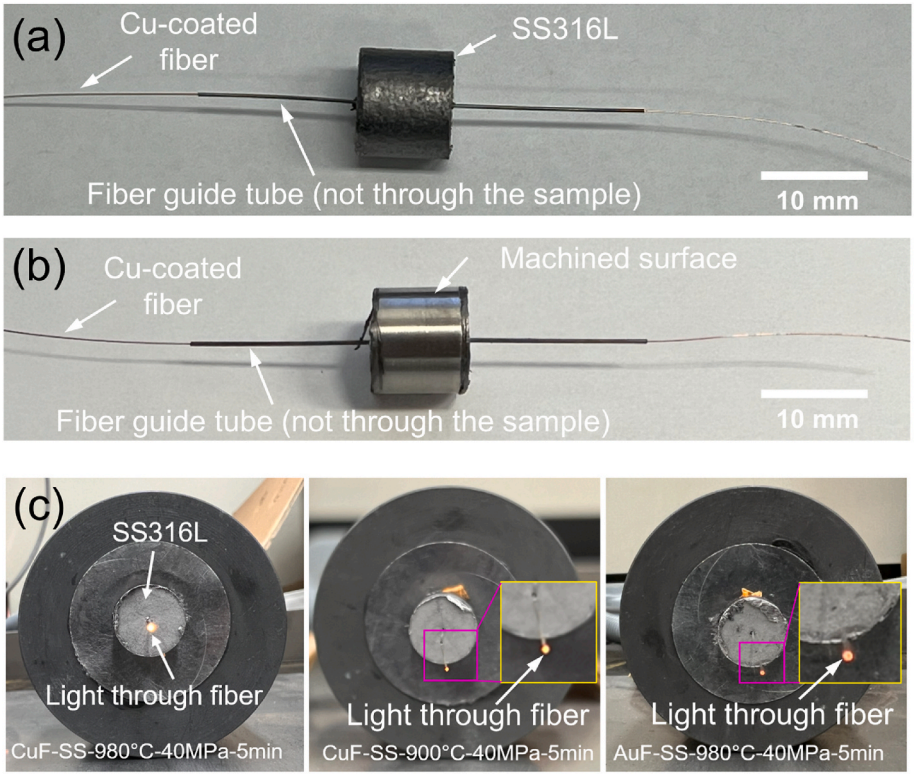

Fig. 4. (a) As-produced and (b) machined SS samples with integrated fiber. (c) Transmission testing of embedded optical fibers in samples fabricated at different conditions.

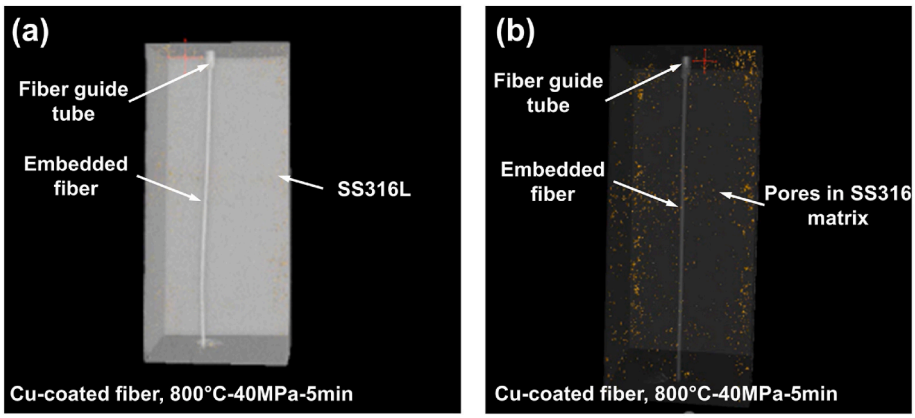

Fig. 5. X-CT scan of a sub-volume of SS with fiber encapsulated at 800 °C to show (a) fiber integrity and (b) pores in the matrix.

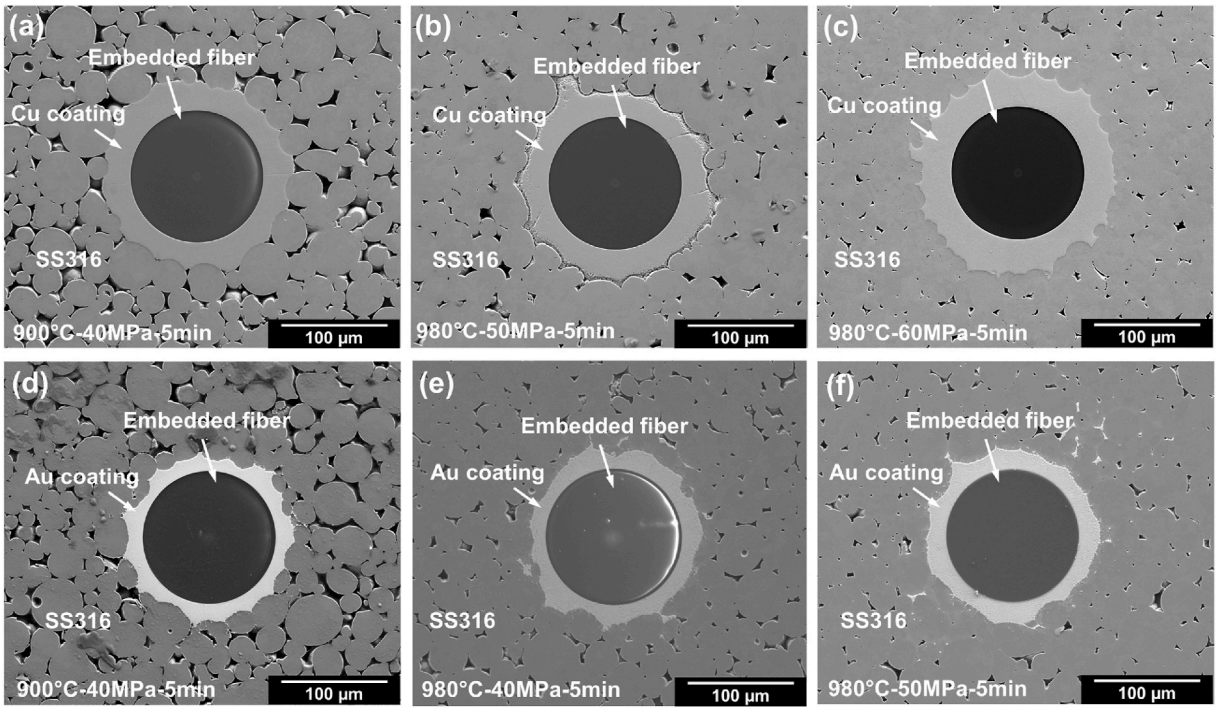

Fig. 6. SEM micrographs illustrating the fiber-matrix interfacial characteristics in the samples with (a–c) Cu-coated and (d–f) Au-coated fibers embedded at various conditions.

this study, two types of commercially available metallized fused silica (SiO_2) optical fiber were selected for embedding. The first type is a copper-coated single mode fiber (Cu1300) from IVG Fiber (Canada). This fiber features a 9 μm diameter Ge-doped core, a 125 μm diameter cladding, and a 165 μm diameter copper coating (with a coating thickness of 20 ± 5 μm). Fig. 1a shows a cross-section of the as-received Cu-coated fiber examined using a scanning electron microscope (SEM, FEI Quanta 650). These fibers exhibit a circular cross-section with a copper alloy coating (specific composition unknown) and are designed for high-temperature applications, tolerating short-term temperature up to 600 °C and long-term temperature up to 450 °C. The Cu-coated fibers also have a thin carbon layer between the silica cladding and the copper coatings. In addition to the Cu-coated fibers, a gold-coated single model fiber (ASI9.0/125/155G) from AMS Technologies (Germany) was tested. As shown in Fig. 1b, the Au-coated fiber has a 9 μm Ge-doped core, a 125 μm pure fused silica cladding, and a 155 μm gold coating (with a coating thickness of 15 ± 5 μm). These fibers are designed to operate in a temperature range of −269 °C–700 °C. Table 1 provides a summary of the specifications for the metallized fibers.

The matrix materials used in this study include stainless steel (SS) 316L and pure nickel. SS was selected due to its extensive use in high-temperature applications, such as heat exchangers, pipes, and pressure vessels, owing to its excellent corrosion resistance and favorable mechanical properties. Nickel and its alloys are similarly employed in high-temperature environments, including applications in aircraft gas turbines, power plants, and nuclear reactors. The SS316L powder used in this study was procured from Carpenter Additive Corporation (USA), while the nickel powder was supplied by American Elements (USA). Both powders were characterized using SEM to analyze their shape and particle size. Fig. 1c and e exhibit the morphology of the SS and nickel powder, respectively. The SS powder consists of a mixture of spherical and irregular shaped agglomerates, whereas the nickel particles primarily comprise spherical particles. Particle size analysis was performed using ImageJ. As shown in Fig. 1d and f, the average particle sizes for SS and nickel were 9.4 μm and 1.9 μm, respectively. The chemical composition of SS316L is provided in Table 2.

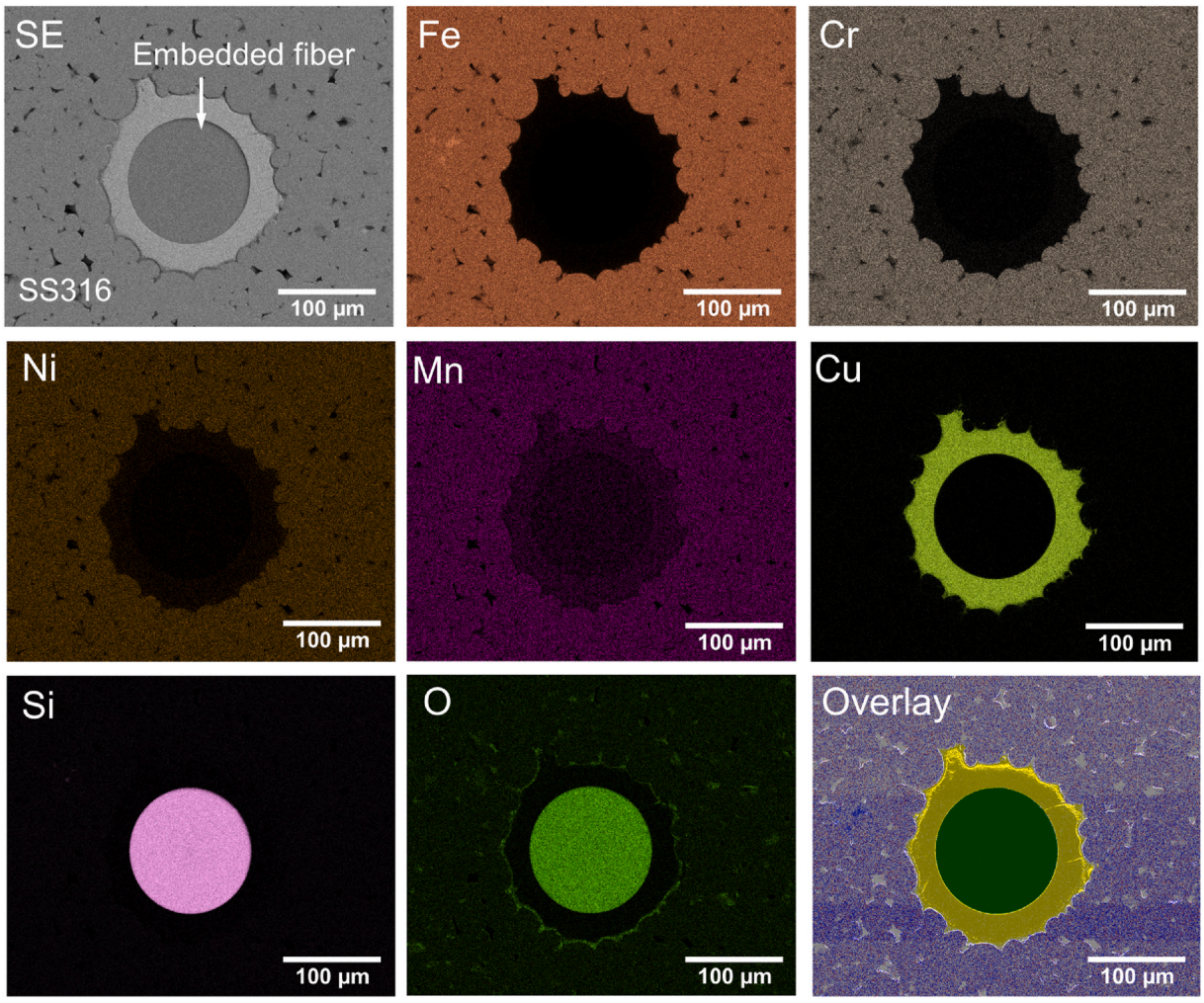

Fig. 7. Elemental distribution maps over SS matrix and embedded Cu-coated fiber.

2.2. Fiber embedding process

Embedding fibers into SS and nickel was achieved using the EFAS technique. EFAS, also known as spark plasma sintering (SPS) or field-assisted sintering technique (FAST), is an advanced manufacturing process that consolidates materials in solid-state by applying high-density electric current and pressure [35]. The electric current induces Joule heating within the materials, enabling rapid heating rates, short processing time, enhanced sintering kinetics, and increased productivity. The short processing time (on the order of minutes) is particularly advantageous for fiber embedding, as the long-term thermal stability of fused silica fibers becomes a concern at temperatures exceeding 1000 °C [37]. Minimizing the exposure of fibers to high temperatures during the embedding process helps to mitigate the attenuation of optical properties. Additionally, EFAS facilitates rapid densification of hard-to-sinter materials, such as composites and ceramics, making it potential for embedding fibers in these materials [35]. In this study, a direct current sintering furnace (DCS-5) from Thermal Technologies, LLC. (USA) was used. This system can deliver up to 2000 amps of current and a load of 5 tons, making it suitable for fabricating samples with diameters ranging from 10 mm to 40 mm.

Fig. 2 illustrates the schematic representation of the embedding procedure. The process began with the preparation of a die assembly consisting of the powder and fiber to be integrated. As shown in Fig. 2a, a 1-mm hole was prepared at the center of the lower graphite punch to facilitate fiber placement. An optical fiber was then vertically inserted into the hole. Next, 7 g of metal powder were loaded into the die to encapsulate the fiber, and the upper punch and spacers were installed to complete the assembly, as depicted in Fig. 2b. A challenge in fiber embedding is preventing fiber breakage at the fiber-sample junctions due to stress concentration. To address this issue, miniature SS316 guide tubes (inner diameter: 0.254 mm, outer diameter: 0.406 mm, and length: 21 mm, 1 mm longer than the punch) were positioned at both the lower and upper junctions. These guide tubes extended ~1 mm into the metal powder, creating a bond during sintering that protected the fiber from breakage at the junctions. Graphite foils were placed at the die-punch-sample interfaces to prevent bonding and ensure easy removal of the sintered sample. Fig. 2c shows a 3D sectional view of the die assembly, illustrating the fiber placement. This setup enabled the embedding of long fibers and allowed for retrieval of the final sintered samples after disassembly. It should be noted that the fibers bended 90° at the upper and lower graphite spacers. The holes on the spacers should be designed to yield to a fiber bending radius larger than the minimum bending radius of fiber to be embedded (10 mm in this study).

The key EFAS parameters influencing material densification include temperature, pressure, and hold time. These parameters were varied over a wide range in this study to explore the relationships between fabrication conditions and embedding properties. Table 3 summarizes the parametric matrix, which covers a temperature range of 800 °C–980 °C, pressure levels between 40 and 50 MPa, and dwell time of 5 and 10 min. These values were scoped based on a literature review of SS316L and nickel materials processed by powder metallurgy [38,39],

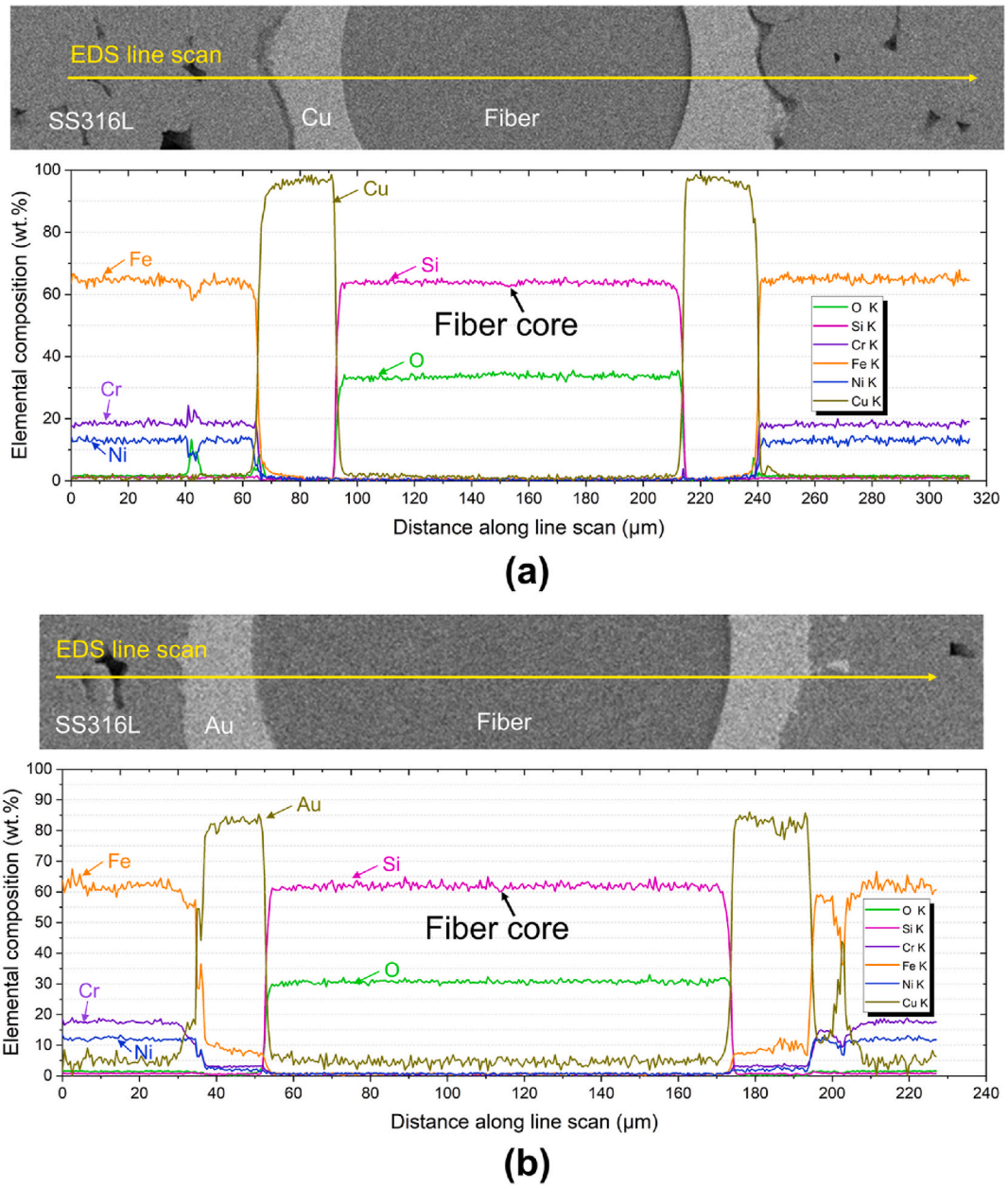

Fig. 8. EDS line scan over the fiber-matrix interface in SS samples with (a) Cu-coated fiber and (b) Au-coated fiber.

Table 4
Helium leak testing results on SS and Ni samples with embedded fibers.

Fiber/ matrix	Sample ID	Embedding condition	Leak test results (Pa)
Cu-coated fiber in SS316L	CuF-SS-900-40-5	900°C-40MPa-5min	Leak – due to interconnected pores at matrix grain boundaries
	CuF-SS-980-50-5 (sample 1)	980°C-50MPa-5min	3.9×10^{-4}
	CuF-SS-980-50-5 (sample 2)	980°C-50MPa-5min	2.1×10^{-5}
Cu-coated fiber in nickel	CuF–Ni-900-50-5	900°C-50MPa-5min	1.7×10^{-7}
	Nickel only (reference)	900°C-50MPa-5min	3.2×10^{-7}

while also accounting for the melting points of the copper (1085 °C) and gold (1064 °C) coatings on the fibers. Temperatures exceeding 1000 °C were avoided, as they caused damage to the metal coatings. A consistent heating rate of 100 °C/min was applied for all experiments, with sample fabrication conducted under an argon atmosphere.

2.3. Optical frequency domain reflectometry

The initial macroscopic inspection of fiber integrity post embedding was conducted by shining light into one end of the fiber and visually examining transmission at the other end. This method allows for a rapid qualitive assessment of the fiber's condition. Fig. 3a illustrates the test setup, where a light source (Fiber-Lite 170D) was coupled to the fiber.

A more detailed evaluation of the embedded fibers was conducted using optical frequency domain reflectometry (OFDR), as shown in the schematic diagram in Fig. 3b. OFDR is an optical technique that analyzes backscattering light (resulting from Rayleigh scattering or FBGs) and optical losses along the entire length of a fiber. The technique involves

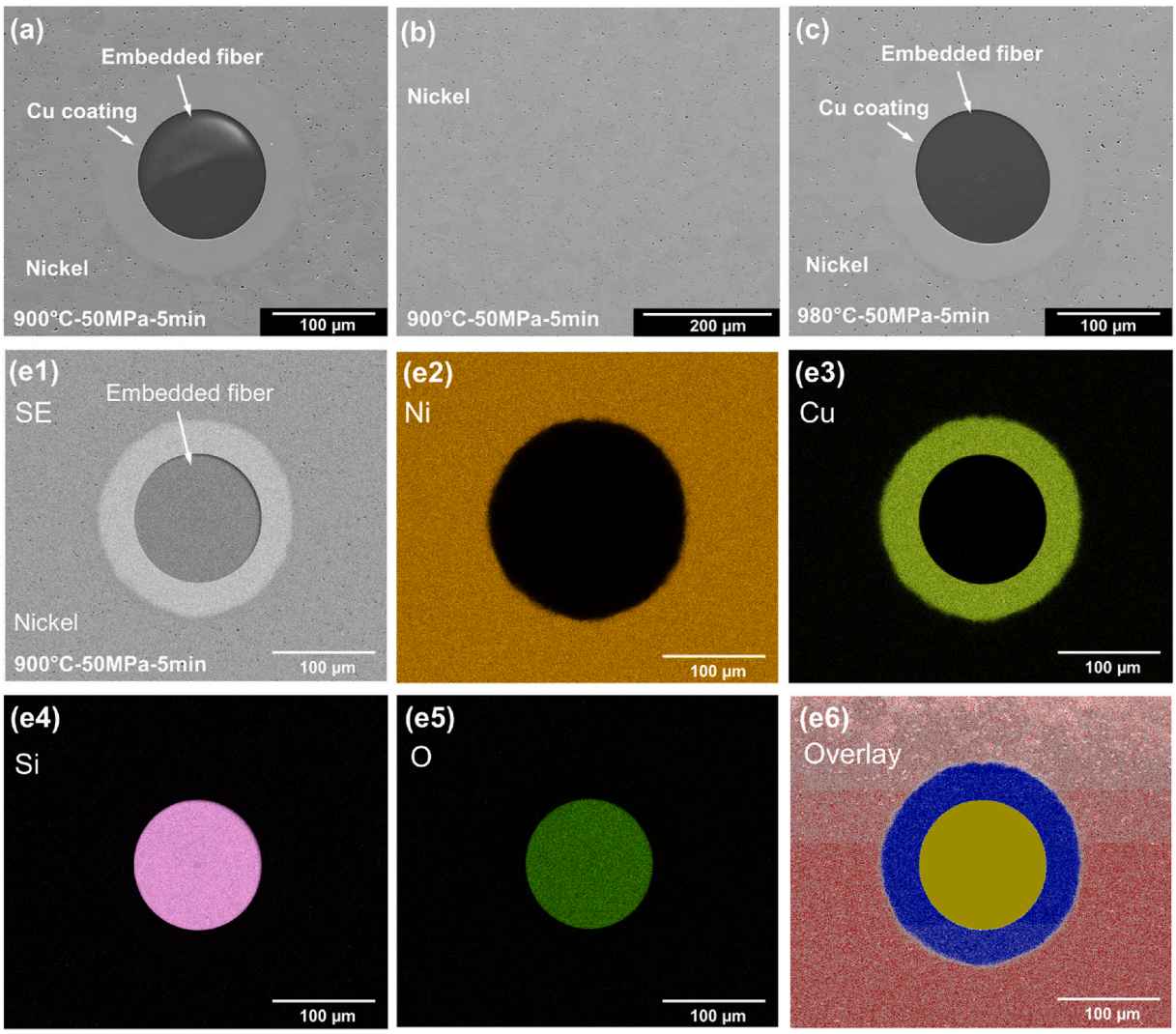

Fig. 9. SEM micrographs showing the (a, c) fiber-matrix bonding area and (b) the nickel matrix. (e1-e6) Elemental distribution maps over the embedded zone.

sending an optical signal through a tunable laser source (TLS), which sweeps across a typical wavelength of 1530–1570 nm. As the signal propagates through a fiber, localized changes in optical properties – due to temperature or strain – generate location-dependent backscattering. This backscattered signal is compared to a reference light, creating an interference pattern. By monitoring variations in the backscattered signal, OFDR allows for the detection of parameters with sub-millimeter spatial resolution.

In this study, the OFDR analysis was performed using an OBR-4600 instrument from Luna Innovations. Fig. 3c shows the splicing of metal-coated fibers with a fiber connector for OBR scan. The fibers were first scanned with the OBR instrument to establish a baseline. Fig. 3c shows an example of the scanned spectrum, where the two peaks denoted the fiber-OBR joint and the end of the fiber. This pre-embedding scan indicated that the last 40 mm of the metal-coated fiber should be avoided to eliminate signal interference with the peak at the fiber end. The scanned fibers were subsequently embedded in SS and nickel using down-selected conditions based on microstructural examinations. Fig. 3d shows a sample with a connector prepared for post-embedding OBR scanning. Fig. 3e depicts the OBR test setup.

2.4. Characterization of the fiber-matrix bond

In-depth characterization of the fiber-matrix bond was achieved using helium leak testing, X-ray computed tomography (X-CT) and advanced microscopy techniques. For the helium leak testing, the as-fabricated samples, originally with an outer diameter of 12 mm, were reduced to 10 mm using a lathe to fit the coupler of the leak testing device. The samples were mounted onto the leak tester and subjected to high vacuum pressure on one side, while the other side was exposed to helium. The steady-state vacuum pressure was recorded to assess the sealing quality.

X-CT was employed to reveal the 3D internal structure of the samples containing embedded fiber. This analysis was performed using a ZEISS Xradia 520 Versa X-ray microscope, which features a tungsten target that generates a cone-beam polychromatic X-ray spectrum. Due to the limited penetrating depth of X-rays, only a sub-volume of the matrix surrounding the fiber was scanned. For microstructural analysis, the as-fabricated samples were sectioned to expose their cross-sections, then mounted and polished following standard metallographic preparation steps. Final polishing was performed to a finish of 0.02 μm using colloidal silica. To prevent sample charging during SEM, the samples were sputtered-coated with gold prior to examination. The samples were examined using SEM to investigate the microstructure and fiber-matrix bond. Elemental distribution was analyzed with an energy-dispersive X-ray spectroscopy (EDS) detector. Elemental mapping and line scans were performed to observe elemental diffusion at the interfaces. A step size of 0.5 μm was used for EDS line scan. Additionally, the grain structure of

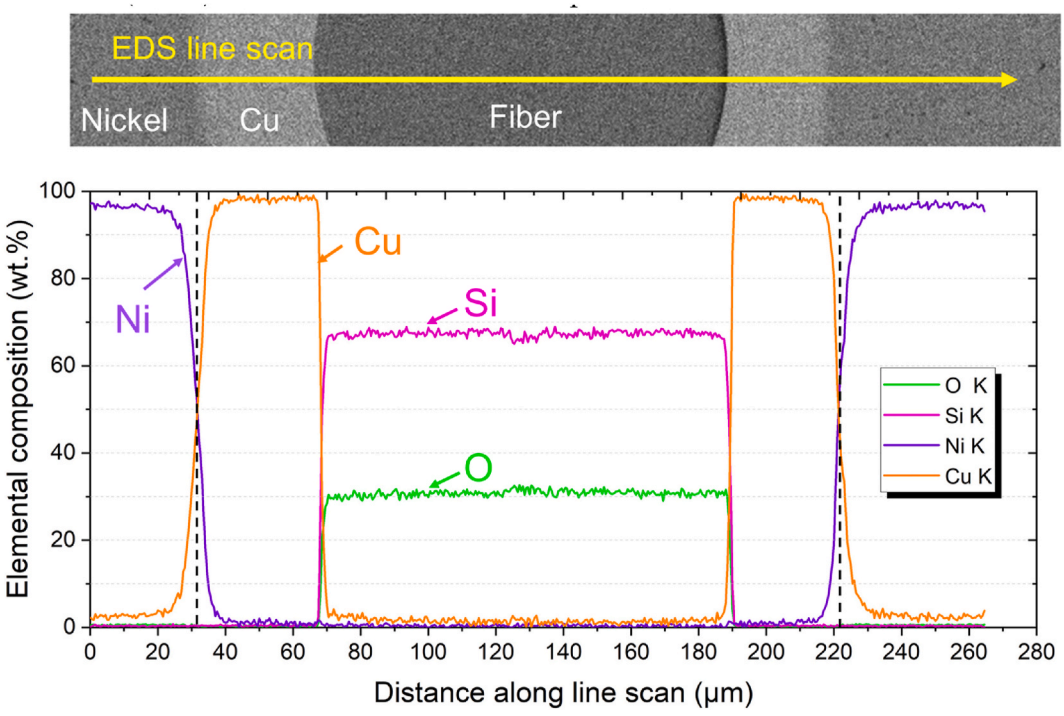

Fig. 10. EDS line scan showing the transition of elements over the fiber-nickel interface.

the samples was revealed using electron-backscattered diffraction (EBSD). EBSD mapping was conducted with a step size of 0.1 μm, and the resulting data was post-processed in OIM Analysis software to exclude datasets with a confidence index of less than 0.1.

2.5. Thermal stability testing

Selected SS and nickel samples with embedded fibers underwent cyclic thermal loading to assess thermal stability. The samples were placed in a tube furnace and subjected to 50 cycles of thermal treatment, with temperatures ranging from 500 °C to 700 °C in air at a heating and cooling rate of 8 °C/min. After cooling to room temperature, the samples were sectioned to reveal their cross-sections, mounted, polished, and examined using SEM. The analysis focused on evaluating fiber integrity and the characteristics of the bonding interface.

3. Results and discussion

3.1. Fiber integrity after embedding

Fig. 4a shows a typical as-fabricated sample with an embedded fiber. The samples were successfully disassembled from the die without damaging the fiber. Notably, the fiber guide tubes, which bonded effectively to the matrix, successfully prevented fiber breakage at the fiber-matrix junctions. The copper and gold coatings retained their integrity at the selected fabrication temperatures (≤980 °C), thereby providing continuous structural support for the silica core and cladding. The outer surface of the sample was covered with graphite foil. Fig. 4b shows a sample with machined surfaces with good geometric tolerance achieved through lathe machining. Importantly, the fiber remained intact post-machining, indicating the basic machinability of the samples with embedded fibers. This characteristic enables the use of these parts as optical feedthroughs, facilitating their integration with parent components for sensing applications. Additionally, the machined surfaces enabled helium leak testing, during which the outer surface was securely clamped to prevent leakage through this region.

The fiber embedding processes, whether utilizing the EFAS method employed in this study or other processes (such as UAM, LPBF, and DED) can introduce residual stress in the encapsulated fibers, potentially leading to failure in light transmission [14,26,40]. To assess whether the embedded fibers remained intact and were capable of transmitting light, a rapid inspection was performed immediately following embedding. This involved shining light into the fiber and visually inspecting the transmitted light. Fig. 4c presents representative examples from the transmission testing, which demonstrates that the fibers remained intact without macroscopic fractures. All samples fabricated according to the parametric matrix (refer to Table 3) passed the visual optical inspection. These findings are consistent with the microstructural analysis discussed in Section 3.2, where all samples exhibited crack-free cross-sections.

Fig. 5 shows an X-CT scan of a SS sample with Cu-coated fiber encapsulated at 800 °C (the animation of the scan is available in the Supplementary Material). The scan confirms the integrity of the fiber post-embedding, showing no signs of discontinuity or cracking. Additionally, the bonding of the fiber guide tube to the matrix is clearly visible. Local bending of the embedded fiber was observed in Fig. 5a. This local bending was caused by the deformation of the matrix during densification. At the sintering temperature, the matrix material experienced deformation due to the consolidation of the metal powder. Bonding between the fiber coatings (Cu or Au) and matrix also occurred at elevated temperatures. As a result, further deformation of the matrix caused local movement of the fiber, resulting in slight bending of the fiber. To minimize fiber local bending, the fiber can be orientated horizontally since the deformation of matrix in radial direction is less compared to the vertical (thickness) direction. However, this may require modification of the die/punch design to allow easy removal of the sample after fabrication.

Fig. 5b displays the scan with adjusted contrast to enhance the visibility of porosity within the sample. The presence of pores is attributed to the low sintering temperature (800 °C). At this condition, SS cannot achieve full densification of the surrounding metal matrix. Typical sintering temperatures required to obtain highly densified SS range from 1000 °C to 1150 °C [38,39,41]. Due to the resolution limit of X-CT, detailed interfacial characteristics between the fiber and matrix were not discernible. Therefore, the samples were sectioned and examined

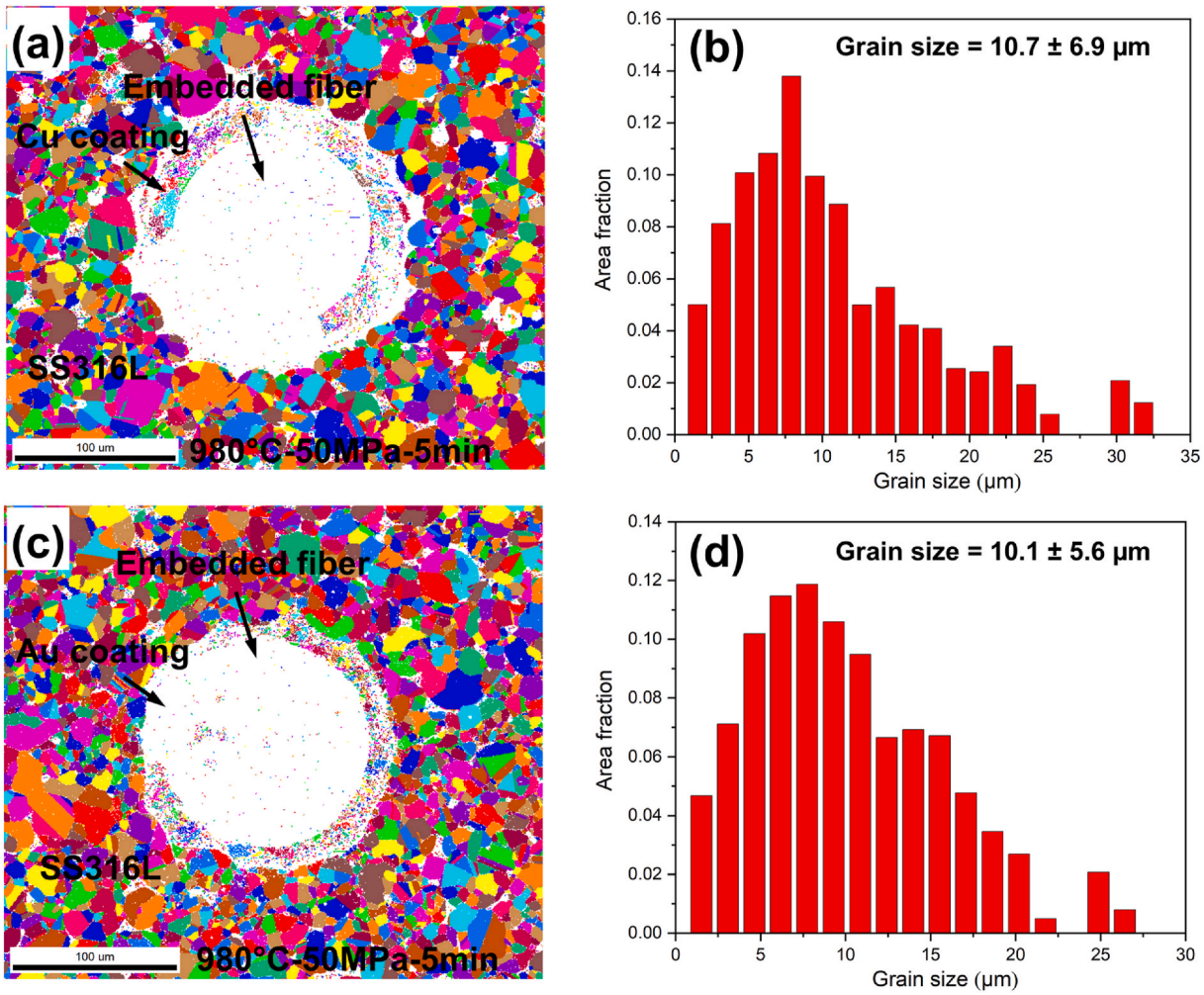

Fig. 11. (a, c) Grain structure and (b, d) grain size statistics of SS with embedded (a, b) Cu-coated fiber and (c, d) Au-coated fiber.

under SEM.

3.2. Fiber-matrix interface characteristics

Samples with embedded fibers were sectioned and analyzed using SEM to reveal the relationships between sample quality – specifically fiber integrity, fiber-matrix bonding, and matrix density – and the processing parameters. Fig. 6 shows representative micrographs of samples fabricated under various conditions. The analysis confirmed the absence of fiber cracking following encapsulation, which is consistent with the results from the transmission test, demonstrating that the fibers have survived the embedding process.

Fig. 6 also indicates the bonding between the metallized fibers and the SS matrix. Some porosities were observed in the matrix, particularly in samples sintered at lower temperatures (≤900 °C). Under suitable fabrication conditions (980 °C), the fiber-matrix bonding was continuous without voids or gaps near the interface (Fig. 6c and f). At this sintering temperature, both copper and gold coatings approached their melting point so soften considerably. The application of pressure during EFAS facilitated the deformation of the fiber coating layer so it could fill any gaps between the SS particles near the interface, resulting in a void-free bond. Such bonding should lead to effective strain coupling between the fiber and the matrix. In contrast to typical embedding microstructures observed in materials processed using UAM [9,42], DED [23–25], and SLM [27,43 where voids are often present at bonding interfaces or fiber failures occur due to unoptimized parameters and experimental setups, the EFAS technique has demonstrated good fiber-matrix integration.

Figs. 7 and 8 illustrate the EDS elemental mapping and line scans performed on SS with embedded fiber where a distinct distribution of primary elements is observed. As shown in Fig. 8a, there is a marked decrease in the major elements of the matrix (Fe, Cr, Ni) as the line scan transitions into the fiber, while the elements of the fiber (Cu, Si, O) reveal abrupt increase. It is worth noticing that elemental diffusion across the matrix and Cu-coatings is evident, indicated by a narrow transition zone (5 ± 0.5 μm) across the interface. This interdiffusion developed during the holding period at the sintering temperature through atomic diffusion across the bi-metallic materials, which indicates the formation of a strong metallurgical bond. Similar interdiffusion of elements during fiber embedding has also been previously reported in UAM studies [13]. Fig. 8b indicates that the diffusion depth (15 ± 0.5 μm) between the SS and Au-coatings is greater than that observed with the Cu-coatings. This phenomenon is attributed to the higher solubility of iron in gold, which allows for the formation of solid solutions based on the Fe–Au phase diagram [44]. In contrast, the mutual solubility of iron and copper is less than 0.1 at.% at room temperature [45]. Nevertheless, it is anticipated that both metal coatings facilitated effective fiber-matrix bonding.

Table 4 summarizes the results of the helium leak tests conducted on selected samples. The SS samples fabricated at lower temperatures (≤900 °C) experienced leaks through the matrix. This is attributed to the open, interconnected pore network formed at low sintering temperatures, (Fig. 6a and d), where helium leaks through the pore network. Increasing the sintering temperature to 980 °C substantially eliminated

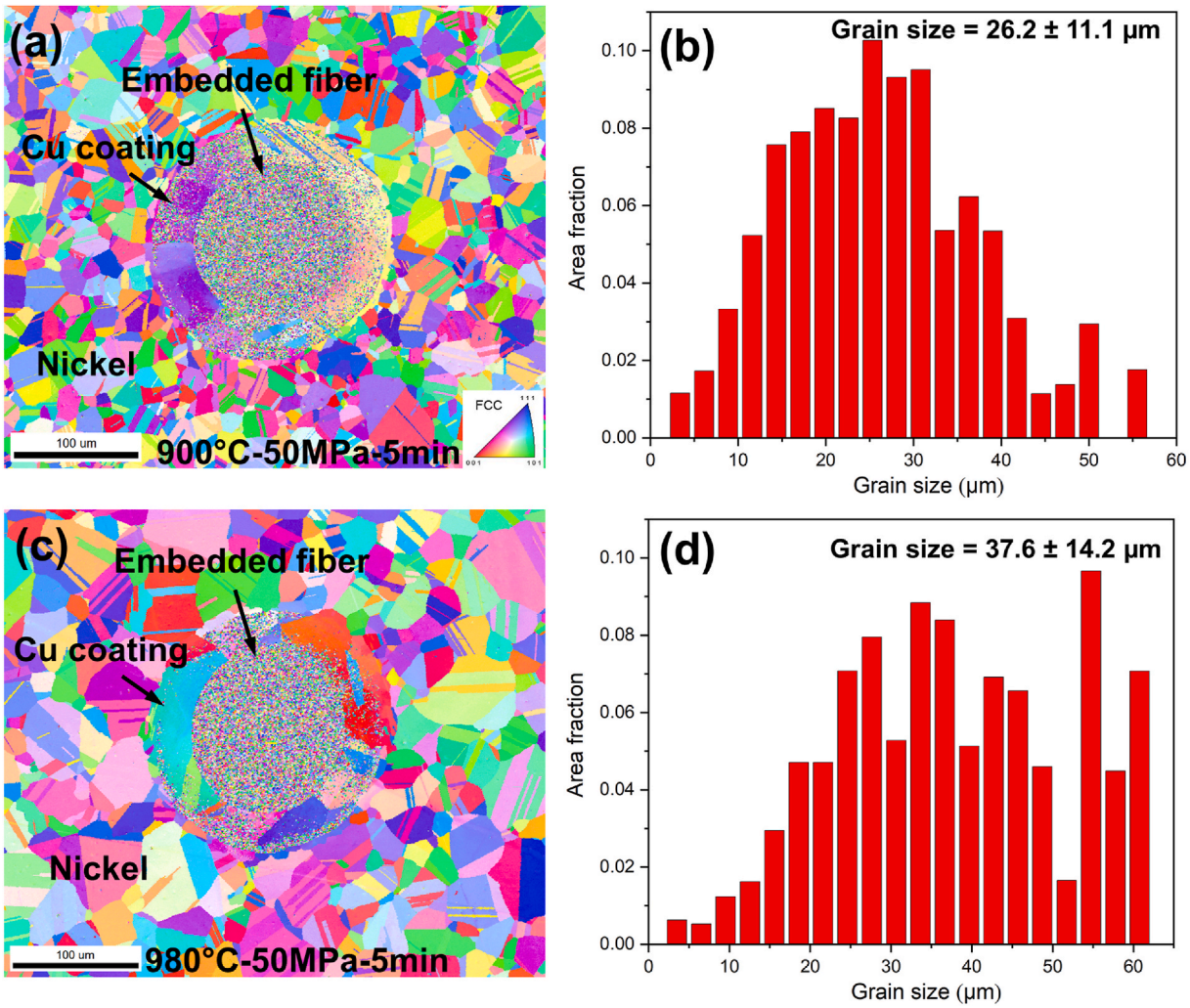

Fig. 12. (a, c) Grain structure and (b, d) grain size statistics of Ni with embedded Cu-coated fiber fabricated at (a, b) 900 °C and (c, d) 980 °C.

the pores, as revealed in Fig. 6b–c, 6e-6f, and Table 3. Consequently, these samples were leak-tight (Table 4). Although further increases in sintering temperature above 1000 °C would enhance pore closure and densification, this is not practical for Cu- and Au-coated fibers due to the risk of melting of the coatings. The absence of metal coatings would result in a loss of structural support for the silica core and cladding, which makes the fiber extremely fragile and non-handleable. Nickel-coated fibers present an ideal alternative due to the nickel's high melting point. With nickel-coatings, sintering temperatures can be elevated to 1200 °C without damaging the nickel layer, facilitating the achievement of fully densified SS. However, nickel-coated optical fibers are rarely available commercially, thus necessitating the development of such coatings through techniques such as electroplating and electroless plating [46]. The exploration of these techniques, however, falls outside the scope of this research.

Fig. 9a–c presents the microstructure of the Ni samples with embedded Cu-coated fibers. Like the SS samples, the fibers maintained their integrity after embedding at both conditions (900°C-50MPa-5min and 980°C-50MPa-5min). The fiber-matrix interface exhibited a high quality of bond. Notably, compared to the SS samples, the Ni samples demonstrated improved densities, even for the sample fabricated at 900 °C which had a density of 98.8% (Fig. 9a–b), a temperature that resulted in large pores and low density (84.3%) in the SS samples (Fig. 6a and d). This observation suggests that pure Ni can achieve better densification at lower temperatures than SS. This is likely due to the presence of alloying elements (Cr and Mo) in SS, which form thin oxide layer on SS powders. While these layers enhance the corrosion and oxidation resistance of SS, they also impede diffusion [47]. The low sintering temperature required for Ni is beneficial for fiber embedding, as it poses less challenges to the fibers. Due to the highly densified microstructure in the Ni samples, they passed the leak test, achieving better vacuum pressure compared to the SS samples, as shown in Table 4. Moreover, the test result for the sample with embedded fiber was comparable to that of the pure Ni, indicating that fiber embedding does not adversely affect sealing capability.

Fig. 9e1-e6 depicts the elemental distribution across the embedded zone. A quantitative transition of elements is plotted in Fig. 10. As anticipated, a well-defined transition zone, 20 ± 0.5 μm wide, was observed at the interface between the Ni matrix and the Cu-coating. Nickel and copper are mutually soluble based on Ni–Cu phase diagram. This mutual solubility facilitates interdiffusion between the two materials. The presence of a transition zone at Ni–Cu interface suggests good fiber-matrix bonding, which is ideal for strain measurement.

3.3. Characteristics of the SS and Ni matrix

A key criterion for successful embedding is the quality of the matrix. In addition to ensuring optimal performance of embedded fibers, a defect-free matrix is essential for providing robust mechanical properties. Therefore, understanding the relationship between embedding parameters and matrix properties is crucial. As illustrated in Fig. 6, the parameters used in the EFAS process, particularly the temperature,

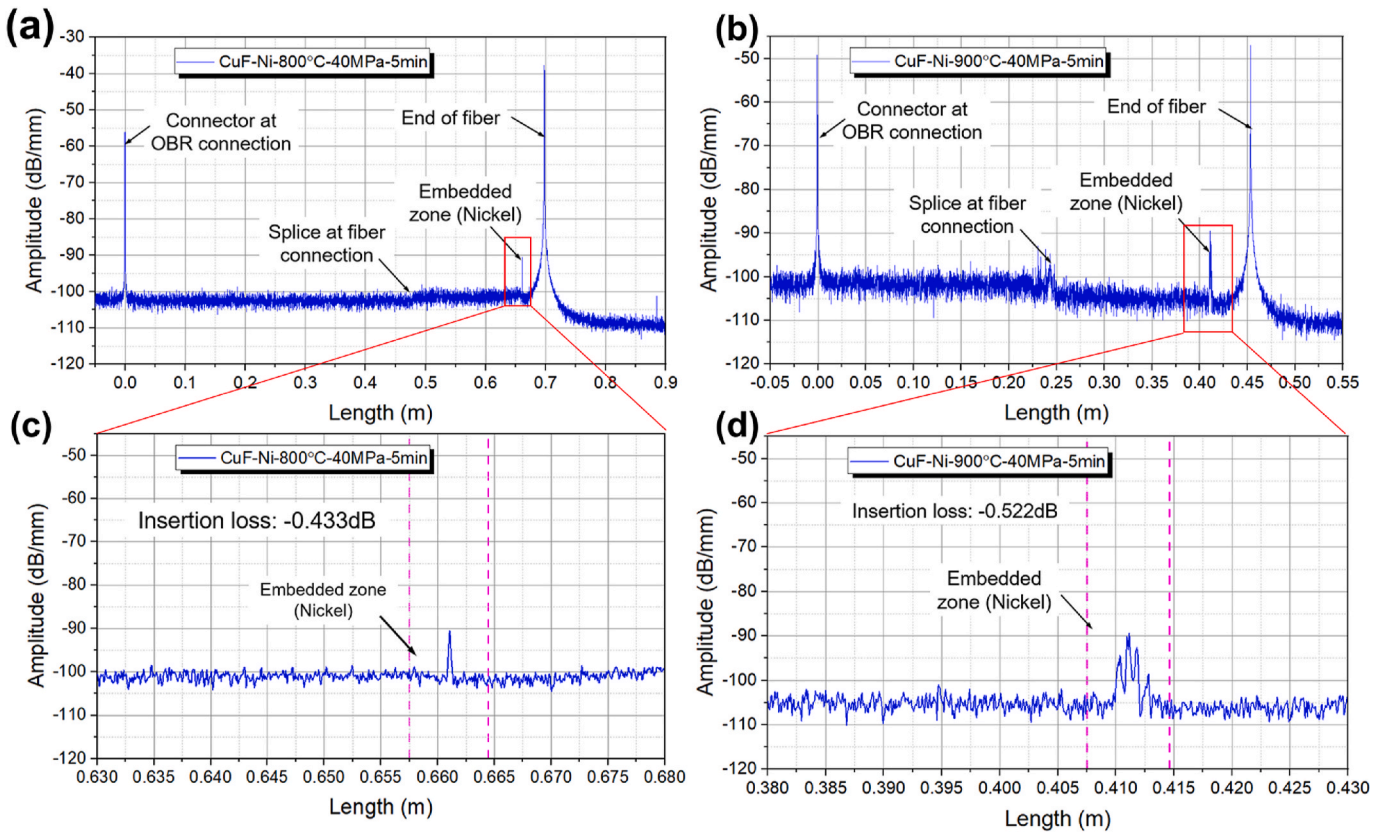

Fig. 13. Rayleigh scattering patterns of the Ni samples with embedded fibers fabricated at (a) 800 °C and 900 °C. (c, d) Magnified view of the patterns near the embedding site.

Table 5
Insertion loss and return loss at the embedding site of the fabricated samples.

Sample ID	Insertion Loss	Return Loss
CuF–Ni-800-40-5	0.43 dB	10.8 dB
CuF–Ni-900-40-5	0.52 dB	9.75 dB
AuF-SS-800-40-5	0.75 dB	15.75 dB
AuF-SS-980-40-5	0 dB	11.19 dB

significantly influence the density of the SS. At low temperatures (≤900 °C), a considerable volume of pores is evident in the matrix (Fig. 6a and d), resulting in low sample density (<85%). Although necking between particles initiated at this stage, the thermal activation was insufficient to eliminate the pores. With increasing temperature and pressure, necking continued to develop while the pores diminished (Fig. 6b–c and 6e-f), leading to improvement of sample density. The sample fabricated at 980 °C and 60 MPa exhibited a density of 97%. Typically, powder sintering encompasses three stages [47]. Stage I is the rearrangement of powders due to applied pressure and particle contact is present but without significant necking and grain boundary formation. As the temperature increases, the process progresses to stage II, where powders come into contact and thermally activated diffusion accelerates, whereby grain boundary and lattice diffusion are primarily associated with pore closure. This stage features a high densification rate. Stage III involves the continuous elimination of pore networks and the growth of grain boundaries, accompanied by a reduced densification rate. The diffusion coefficient is largely driven by temperature and can be expressed as [48]:

$$D = D_0 \exp\left(\frac{Q}{RT} + \frac{A|Z^*|etj}{RT}\right) \quad (1)$$

where D_0 is the material constant, Q is the energy of formation of vacancies, R is the gas constant, T is the temperature, A is the constant, Z^* is the effective valence, e is the charge of an electron, t is the resistivity, and j is the current density. The diffusion coefficient increases with the increase of temperature. It should also be mentioned that in contrast to traditional sintering techniques utilizing induction furnaces, EFAS applies electric current into the materials, which can accelerate diffusion based on Eq. (1). As such, EFAS enables the sintering of materials at lower temperatures with a much shorter time compared to conventional sintering methods [35]. This is preferred for fiber embedding as it helps mitigate changes in optical property that can occur at extreme temperatures.

Fig. 11 reveals the grain morphologies and corresponding grain size statistics of the SS with Cu- and Au-coated fibers fabricated at the same condition. Since fused silica fibers are amorphous, they appear as non-indexed points in the EBSD maps (Fig. 11a and c). The SS exhibited refined and equiaxed fcc (face-centered cubic) austenitic grains, with an average grain size of ~10 μm. Such fine grains are typically seen in materials processed by EFAS, which is attributed to the rapid heating and short processing time [49]. According to the Hall-Petch relationship, smaller grains can enhance the mechanical strength of materials through grain boundary strengthening. Previous studies have reported that materials fabricated by EFAS often exhibit better tensile strength compared to those produced by other sintering techniques [12,47]. However, it should be noted that the SS samples in this study contained pores within the matrix as the temperature cannot be further increased without melting the fiber coatings. These pores may compromise the mechanical properties of the materials. Thus, tensile testing is worth of conducting on the SS samples to reveal the strength and ductility of the material.

Fig. 12 depicts the grain structure of the Ni samples fabricated at different temperatures. The Ni matrix exhibited equiaxed grains with

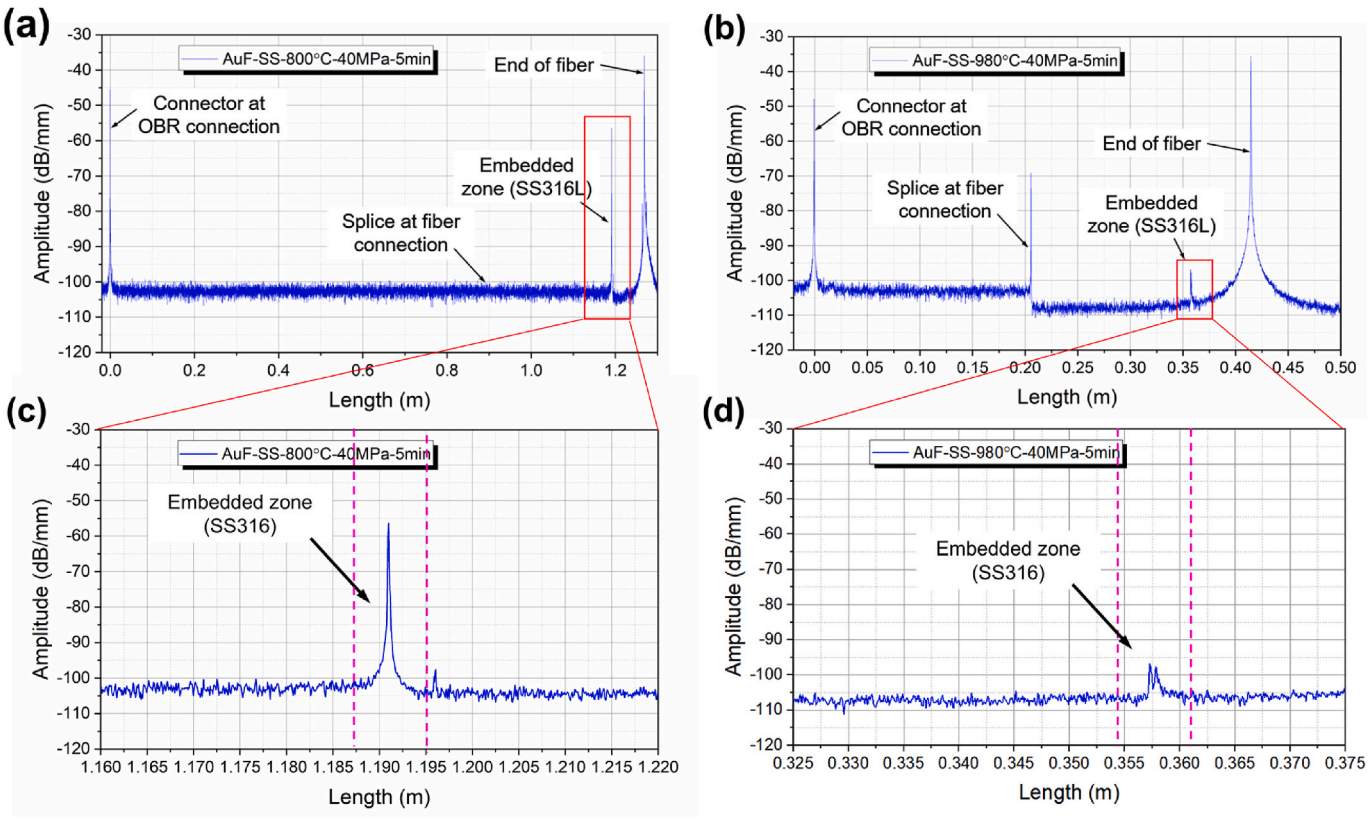

Fig. 14. Rayleigh scattering patterns of the SS samples with embedded fibers fabricated at (a) 800 °C and 980 °C. (c, d) Magnified view of the patterns near the embedding site.

annealing twins. A grain size of 26.2 ± 11.1 μm was obtained in the Ni produced at 900 °C. This grain size is relatively large considering the fine particle size of the powder (1.9 μm). This indicates that significant grain growth occurred at the sintering temperature of 900 °C. This finding suggests that the sintering temperature for Ni could potentially be lowered while still achieving a well-densified matrix. Additionally, Fig. 12 shows that as the sintering temperature increases, further grain growth occurred. The Ni sintered at 980 °C exhibited coarse grains compared to that at 900 °C. This implies that further increasing the temperature above 900 °C is unnecessary for densifying Ni but may lead to grain growth. This can also be revealed from the density measurements that both the Ni samples fabricated at 900 °C and 980 °C exhibited same density of 98.8% (Table 3). In terms of the mechanical strength of pure Ni, a previous study has shown that pure Ni has a yield strength between 230 and 300 MPa and an ultimate tensile strength between 560 and 640 MPa (grain size of 5 μm) [50].

3.4. Optical properties of embedded fibers

Fig. 13a and b shows the OBR scanned spectrums of the fibers embedded in Ni obtained at 800 °C and 900 °C, respectively. The first main peak (length = 0) in the spectrums denotes the connector at the fiber-OBR interface, while the second large peak results from the reflection at the end of the fiber. Additionally, a peak in the embedded zone is observed adjacent to the end-of-fiber peak. Fig. 13c and d shows a magnified view of the spectrums near the embedded zone. From these scans, the insertion loss and return loss at the embedding site can be determined. Insertion loss (lower values are preferable) quantifies the loss of signal during transmission along the fiber, whereas return loss (higher values are preferable) measures the amount of signal reflected toward the source. The measurements indicate insertion loss of 0.43 dB and 0.52 dB for the fiber embedded in Ni at 800 °C and 900 °C, respectively, as listed in Table 5. These levels of insertion loss are minimal and comparable to the loss at a clean fiber connection. Furthermore, these values are lower than the losses observed in Al-/Cu-coated fibers integrated in Al-3003 by UAM (~2 dB) [14], Cu-coated fiber embedded in Al-6961 (2 dB) [40], and fibers embedded in alumina by extrusion printing (2.5–1.0 dB) [51]. The low insertion loss associated with embedding via EFAS indicates good optical properties of the fiber once encapsulated in the metals. Return loss was calculated from the OFDR spectrum using equation (2) [52]:

$$RL = -10\log(P_{ST}) = -10\log\left(\frac{P_0 - P_B}{P_1 - P_B}(P_2 - P_B) - \frac{(P_0 - P_B)}{2}\right) \quad (2)$$

where is P_0 the signal power at the fiber section before the embedding site, P_B is the background noise level, P_1 is the signal power just prior to the reflection event (embedding site), and P_2 is the signal power returned from the reflection at the embedding zone. The return loss at the embedding site was calculated to be 10.8 dB and 9.75 dB for the Ni fabricated at 800 °C and 900 °C, respectively (Table 5). This indicated that 8.3% (Ni-800 °C) and 10.6% (Ni-900 °C) of signal launched at the point of the embedding site was reflected. The insertion loss of 0.43 dB and 0.52 dB revealed that 90.6% (Ni-800 °C) and 88.7% (Ni-900 °C) of power launched was transmitted through the embedding site. The calculation for insertion loss and return loss confirms the absence of losses outside of the fiber, which indicates that the return loss is a result of Fresnel reflection due to strain at the embedding site. This strain leads to change in the refractive index of the fiber in the embedding site, which caused the peak observed in the OBR spectrums.

The EFAS temperature was found to influence both the insertion loss and return loss. Specifically, lower sintering temperatures resulted in reduced insertion loss and increased return loss, which is preferred as it exerts less impact on the optical fiber. The effect of temperature on optical properties is attributed to strain induced during the embedding process. At higher sintering temperatures, the matrix experienced more

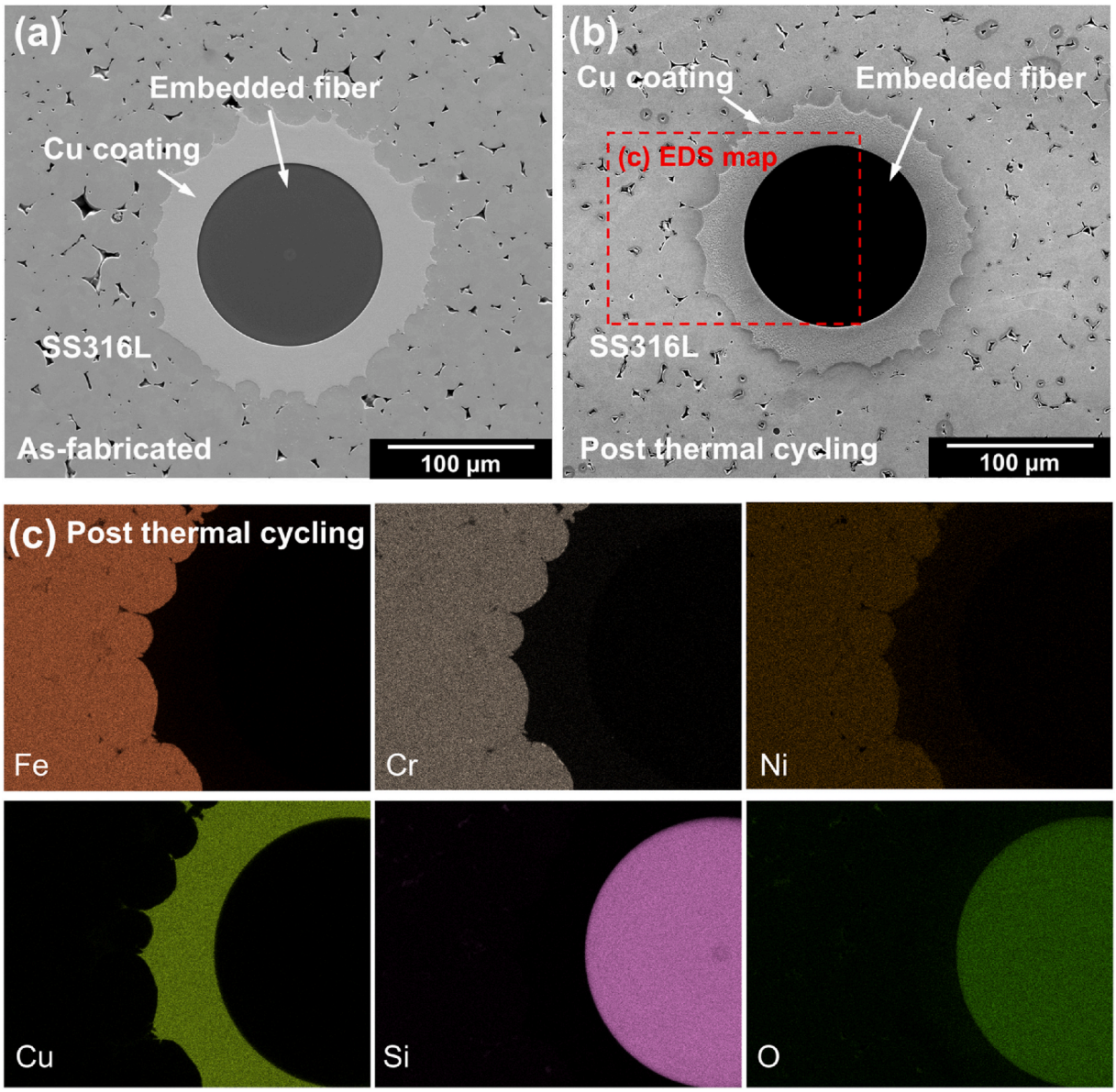

Fig. 15. SEM micrographs showing interface characteristics of (a) as-fabricated and (b) post-thermal-cycled SS with embedded Cu-coated fiber (fabricated at 980°C-50MPa-5min). (c) Distribution of elements in the SS sample after thermal cycling.

densification and deformation due to enhanced diffusion between metal particles and the closure of pores. Upon cooling, the mismatch of the coefficient of thermal expansion (CTE) between the matrix (13.1×10^{-6}/°C for Ni) and fiber (0.55×10^{-6}/°C for silica) also contributed to high residual stress on the fibers. Consequently, samples fabricated at higher temperatures experienced higher local mechanical stress on the embedded fiber. This mechanical stress locally altered the index of refraction of the fiber, leading to higher insertion loss.

Fig. 14a and b presents the Rayleigh scattering patterns of the SS samples with embedded Au-coated fibers. Similar to the patterns observed in the Ni samples, the two main peaks correspond to reflection at the fiber-OBR connection and the end of the fiber. Fig. 14c and d shows a magnified view of the embedded region. The insertion losses for the SS samples fabricated at 800 °C and 980 °C were determined to be 0.75 dB and 0 dB, respectively. Notably, the fiber embedded in SS produced at 980 °C revealed full signal transmission through the fiber. In contrast, the fiber embedded at 800 °C exhibited greater signal attenuation. The trend of insertion loss as a function of fabrication temperature observed in the SS samples differs from that seen in the nickel samples. This discrepancy may result from local strain conditions and changes in the refractive index after embedding. The calculation of return loss and insertion loss for the SS made at 800 °C indicates that 14% of light was lost from the fiber, while the sample made at 980 °C showed minimal transmission loss. This may suggest that the fiber embedded at 800 °C experienced more localized microscopic deformation, which affected its refractive index. Nevertheless, OFDR measurements confirm that fibers embedded in SS at both temperatures successfully transmitted light with acceptable levels of attenuation.

Embedding process can result in residual strain on embedded fiber. For example, it was reported that fibers embedded via UAM and LPFB have a compressive strain of ~2000 μm/m [9] and ~3500 μm/m [26] at room temperature. Maintaining a compressive strain after embedding is critical to ensure good fiber integrity at high temperatures 53. Residual strain in embedded fiber can be revealed using FBG or Rayleigh scattering methods [9,26]. Revealing residual strain in EFAS-embedded fibers using these methods is worth pursuing to advance this fiber encapsulation technology for high-temperature sensing applications.

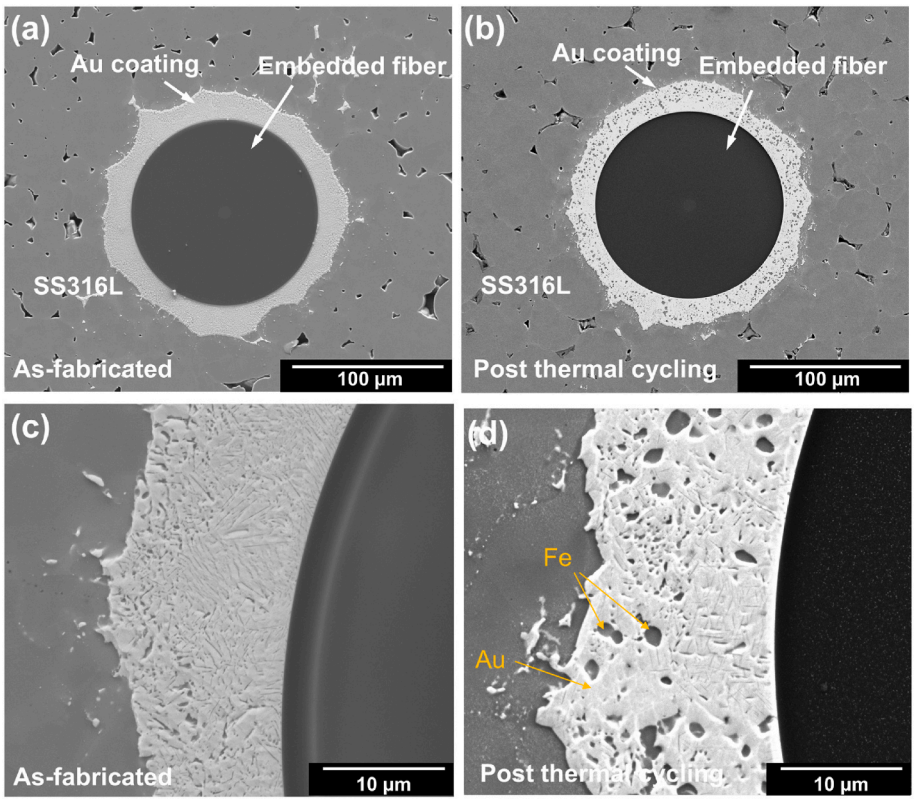

Fig. 16. SEM micrographs showing interface characteristics of (a, c) as-fabricated and (b, d) post-thermal-cycled SS with embedded Au-coated fiber (fabricated at 980°C-50MPa-5min).

3.5. Interface characteristics after cyclic thermal treatment

Fig. 15a and b shows the microstructure of a SS sample with embedded Cu-coated fiber before and after 50 cycles thermal treatment between 500 and 700 °C. The results demonstrate that the fibers remained intact following the thermal treatment, indicating their good thermal stability. Compared to the microstructure before thermal cycling, the interfacial characteristics revealed no obvious changes. A defect-free metallurgical bond was still evident after thermal cycling, as shown in Fig. 15c.

In comparison to fibers embedded using UAM which have been reported to develop de-bonding between the coating and matrix after heat treatment at 400 °C and fiber failure at 500 °C [42], the samples processed by EFAS maintained both fiber integrity and fiber-matrix bonding after thermal cycling. This difference may be attributed to the distinct thermal histories encountered during embedding in UAM and EFAS processes. UAM is a low temperature embedding technique that relies on high energy vibrations and plastic deformation to join materials. When these samples are heated to high temperatures during heat treatment, excessive stress can develop in the embedded region due to the CTE mismatch between the fiber and matrix. Such excessive stress can lead to delamination of the fiber from the matrix and ultimately result in fiber failure. In contrast, EFAS embeds fibers at high temperatures. At the target sintering temperature, stress is applied to the fiber through the EFAS pressure. Upon cooling to room temperature, additional stress on the embedded fiber arises from the fiber-matrix material mismatch. This stress can attenuate the optical properties of the fiber, as observed in the OFDR scans. When the sample was subsequently reheated, stress relief occurred at the fiber-matrix interface, alleviating the stress on the fibers and preventing debonding from the matrix.

Fig. 16 illustrates the interfacial characteristics of the SS samples with embedded Au-coated fibers. Compared to the as-fabricated sample, the thermally cycled sample exhibits a greater clustering of diffused elements within the gold coatings. Increased quantities of iron islands were seen in the coatings, which was a consequence of elemental diffusion during cycling at elevated temperatures. Despite these changes, effective bonding was maintained after thermal cycling, confirmed by the bi-material interdiffusion. Analysis of the interface of the nickel samples was also conducted. The characterization indicates similar interfacial characteristics compared to the sample before thermal treatment.

It can be observed from Figs. 15 and 16 that the porosities in the samples reduced after thermal cycling. This may indicate further diffusion of materials and pore closure during thermal treatment. Diffusion is largely a thermal-driven process, during which high temperatures induce atomic diffusion, leading to pore closure. This suggests that thermal treatment on as-fabricated samples can further enhance material densification. However, the degree of densification from thermal treatment alone is limited due to the absence of applied pressure, which is also needed to close the pores and facilitate successful consolidation.

4. Conclusions

The unique characteristics of fiber optic sensors make them very attractive for sensing applications in harsh environments. Embedding these sensors in structural materials is a crucial step for effective sensing and health monitoring. Successful fiber embedding requires achieving a good fiber-matrix bond without interfacial defects, maintaining fiber integrity and functionality, and preserving these properties during high-temperature service. This study demonstrates the use of electric current assisted sintering technique to embed fused silica fiber optic sensors in SS316L and nickel. Copper-coated and gold-coated optical fibers were arranged in stainless steel and nickel powders which were sintered using EFAS technology under various conditions. A systematic inspection was conducted to assess the embedding quality, including helium leak tests and microstructural analysis using advanced microscopy to evaluate

fiber-matrix bonding, optical property measurement via OFDR, machinability testing, and evaluation of embedding properties after 50 thermal cycles between 500 and 700 °C. The results indicate that the fibers remained intact after embedding with the selected parameters. A good metalogical bond between the fiber and matrix, with elemental interdiffusion across the interface, was achieved. Both SS and nickel samples with embedded fibers passed the helium leak test, with the nickel samples showing better results due to improved densification. OFDR scans revealed insertion losses of 0.43 dB and 0.52 dB for the nickel samples fabricated at 800 °C and 900 °C, respectively. These insertion losses were attributed to Fresnel reflection caused by residual strain on the fibers at the embedding sites. More aggressive fabrication conditions led to higher residual stress on the fibers, resulting in greater optical attenuation. After thermal cycling, the fibers embedded in both SS and nickel remained intact. Thermal-cycled SS sample with Cu-coated fiber and nickel sample with Cu-coated fiber exhibited similar interfacial characteristics compared to the as-fabricated samples. However, the SS samples with Au-coated fibers showed more material diffusion and clustering at the interface after thermal cycling.

Several areas could be addressed to further advance the embedding technology. One area is the fabrication of near-net shaped components with embedded sensors. This involves advancing the EFAS technology itself and minimizing local fiber bending that may occur during embedding. Near-net shaping minimizes the need for extensive machining, which can be difficult because of the embedded optical fiber. Moreover, controlling local fiber bending is important to enhance the accuracy and reliability of measurements. In addition, investigating and controlling residual strain after embedding is critical to ensure good sensing functionalities. Addressing these challenges will be pivotal for the further development and successful deployment of EFAS technology for fiber embedding for high-temperature SHM.

Declaration of competing interest

The authors declare that they have no known competing financial interests or personal relationships that could have appeared to influence the work reported in this paper.

Acknowledgments

This project was funded by the Advanced Sensors and Instrumentation (ASI) program from the U.S. Department of Energy (DOE) Office of Nuclear Energy (NE) under the Department of Energy (DOE) Idaho Operations Office Contract DE-AC07-05-ID14517.

Appendix A. Supplementary data

Supplementary data to this article can be found online at https://doi.org/10.1016/j.jmrt.2024.12.050.

References

[1] Liu Y, Nayak S. Structural health monitoring: state of the art and perspectives. JOM 2012;64(7):789–92.
[2] Zhang S, Cao R, Jia Z, Xiong Y, Chen C, Zhang Y. Cement/epoxy-based embedded ultrasonic transducers for concrete structure applications. J Mater Res Technol 2021;14:242–54.
[3] De Giorgi MG, Menga N, Ficarella A. Exploring prognostic and diagnostic techniques for jet engine health monitoring: a review of degradation mechanisms and advanced prediction strategies. Energies 2023;16(6):2711.
[4] Martinez-Luengo M, Kolios A, Wang L. Structural health monitoring of offshore wind turbines: a review through the Statistical Pattern Recognition Paradigm. Renew Sustain Energy Rev 2016;64:91–105.
[5] Daw JE, Good M, Meyer R, Ramuhalli P, Breon L. In: Medium, editor. Assessment of acoustic sensor application to structural health monitoring of reactor components. United States: Size; 2022. p. 33.
[6] Sun B, Fu W, Luo Y, Zhao W. Development of internal moisture transfer and cumulative residual strain in concrete under freeze-thaw cycles. J Mater Res Technol 2022;20:1243–54.
[7] Sabri N, Aljunid SA, Salim MS, Fouad S. Fiber optic sensors: short review and applications. In: Gaol FL, Shrivastava K, Akhtar J, editors. Recent trends in physics of material science and technology. Singapore: Springer Singapore; 2015. p. 299–311.
[8] Raghavan A, Kiesel P, Sommer LW, Schwartz J, Lochbaum A, Hegyi A, Schuh A, Arakaki K, Saha B, Ganguli A, Kim KH, Kim C, Hah HJ, Kim S, Hwang G-O, Chung G-C, Choi B, Alamgir M. Embedded fiber-optic sensing for accurate internal monitoring of cell state in advanced battery management systems part 1: cell embedding method and performance. J Power Sources 2017;341:466–73.
[9] Hyer HC, Sweeney DC, Petrie CM. Functional fiber-optic sensors embedded in stainless steel components using ultrasonic additive manufacturing for distributed temperature and strain measurements. Addit Manuf 2022;52:102681.
[10] Datta A, Augustin MJ, Gaddikeri KM, Viswamurthy SR, Gupta N, Sundaram R. Damage detection in composite aircraft wing-like test-box using distributed fiber optic sensors. Opt Fiber Technol 2021;66:102651.
[11] Witt J, Narbonneau F, Schukar M, Krebber K, Jonckheere JD, Jeanne M, Kinet D, Paquet B, Depre A, Angelo LTD, Thiel T, Logier R. Medical textiles with embedded fiber optic sensors for monitoring of respiratory movement. IEEE Sensor J 2012;12(1):246–54.
[12] Zhang X, Hua Z, Picklesimer CA, Chuirazzi WC, Sun C, McMurtrey MD, Rufner J. Integrating fiber optic sensors into metallic components for sensing in harsh environments. Opt Laser Technol 2024;170:110188.
[13] Pagan M, Petrie C, Leonard D, Sridharan N, Zinkle S, Babu SS. Interdiffusion of elements during ultrasonic additive manufacturing. Metall Mater Trans 2021;52(3):1142–57.
[14] Monaghan T, Capel AJ, Christie SD, Harris RA, Friel RJ. Solid-state additive manufacturing for metallized optical fiber integration. Compos Appl Sci Manuf 2015;76:181–93.
[15] Schomer JJ, Dapino MJ. High temperature characterization of fiber Bragg grating sensors embedded into metallic structures through ultrasonic additive manufacturing. In: ASME 2017 conference on smart materials, adaptive structures and intelligent systems; 2017.
[16] Schomer J, Hehr A, Dapino M. Characterization of embedded fiber optic strain sensors into metallic structures via ultrasonic additive manufacturing, SPIE. 2016.
[17] Hehr A, Norfolk M, Wenning J, Sheridan J, Leser P, Leser P, Newman JA. Integrating fiber optic strain sensors into metal using ultrasonic additive manufacturing. JOM 2018;70(3):315–20.
[18] Sweeney DC, Schrell AM, Petrie CM. Pressure-driven fiber-optic sensor for online corrosion monitoring. IEEE Trans Instrum Meas 2021;70:1–10.
[19] He XL, Wang ZQ, Wang DH, Wang XB, Liu Y, Jiang FC, Yuan LB. Optical fiber sensor for strain monitoring of metallic device produced by very high-power ultrasonic additive manufacturing. IEEE Sensor J 2019;19(22):10680–5.
[20] Chilelli SK, Schomer JJ, Dapino MJ. Detection of crack initiation and growth using fiber Bragg grating sensors embedded into metal structures through ultrasonic additive manufacturing. Sensors 2019;19(22):4917.
[21] Zhao J, Dong W, Hinds T, Li Y, Splain Z, Zhong S, Wang Q, Bajaj N, To A, Ahmed M, Petrie CM, Chen KP. Embedded fiber Bragg grating (FBG) sensors fabricated by ultrasonic additive manufacturing for high-frequency dynamic strain measurements. IEEE Sensor J 2024;24(3):2853–62.
[22] Wang B, Zhang H, Gao C, Lv W. Microstructure and mechanical properties of Ti/Al laminates fabricated by ultrasonic additive manufacturing assisted by Joule heat and post-welding heat treatment. J Mater Res Technol 2023;27:2149–65.
[23] Grandal T, Zornoza A, Fraga S, Castro G, Sun T, Grattan KTV. Laser cladding-based metallic embedding technique for fiber optic sensors. J Lightwave Technol 2018;36(4):1018–25.
[24] Zou R, Liang X, Chen Q, Wang M, Zaghloul MAS, Lan H, Buric MP, Ohodnicki PR, Chorpening B, To AC, Chen KP. A digital twin approach to study additive manufacturing processing using embedded optical fiber sensors and numerical modeling. J Lightwave Technol 2020;38(22):6402–11.
[25] Kim SI, Jung HY, Yang S, Yoon J, Lee H, Ryu W. 3D Printing of a miniature turbine blade model with an embedded fibre Bragg grating sensor for high-temperature monitoring. Virtual Phys Prototyp 2022;17(2):156–69.
[26] Hyer HC, Petrie CM. Distributed strain sensing using Bi-metallic coated fiber optic sensors embedded in stainless steel. Addit Manuf 2024;91:104355.
[27] Mathew J, Havermann D, Polyzos D, MacPherson W, Hand D, Maier R. SS316 structure fabricated by selective laser melting and integrated with strain isolated optical fiber high temperature sensor, SPIE. 2015.
[28] Havermann D, Mathew J, MacPherson W, Hand D, Maier R. Measuring residual stresses in metallic components manufactured with fibre Bragg gratings embedded by selective laser melting, SPIE. 2015.
[29] Petrie CM, Schrell AM, Leonard DN, Yang Y, Jolly BC, Terrani KA. Embedded sensors in additively manufactured silicon carbide. J Nucl Mater 2021;552:153012.
[30] Li D. A review of microstructure evolution during ultrasonic additive manufacturing. Int J Adv Des Manuf Technol 2021;113(1):1–19.
[31] Kuo C-H, Sridharan N, Han T, Dapino MJ, Babu SS. Ultrasonic additive manufacturing of 4130 steel using Ni interlayers. Sci Technol Weld Join 2019;24(5):382–90.
[32] Han T, Kuo C-H, Sridharan N, Headings LM, Babu SS, Dapino MJ. Effect of preheat temperature and post-process treatment on the microstructure and mechanical properties of stainless steel 410 made via ultrasonic additive manufacturing. Mater Sci Eng, A 2020;769:138457.
[33] Levy A, Miriyev A, Sridharan N, Han T, Tuval E, Babu SS, Dapino MJ, Frage N. Ultrasonic additive manufacturing of steel: method, post-processing treatments and properties. J Mater Process Technol 2018;256:183–9.

[34] Philipp Stoll Adriaan Spierings TBJM, Maier Robert RJ, Wegener Konrad. Embedding fibre optical sensors into SLM parts, Solid Freeform Fabrication 2016. Proceedings of the 26th Annual International 2016:1815–25.
[35] Guillon O, Gonzalez-Julian J, Dargatz B, Kessel T, Schierning G, Räthel J, Herrmann M. Field-assisted sintering technology/spark plasma sintering: mechanisms, materials, and technology developments. Adv Eng Mater 2014;16(7):830–49.
[36] Liu B, Yu Z, Hill C, Cheng Y, Homa D, Pickrell G, Wang A. Sapphire-fiber-based distributed high-temperature sensing system. Opt Lett 2016;41(18):4405–8.
[37] Homa D, Pickrell G, Wang A. Investigation of high temperature silica based fiber optic materials, United States. 2018. Medium.
[38] Yang J, Trapp J, Guo Q, Kieback B. Joining of 316L stainless steel by using spark plasma sintering method. Mater Des 2013;52:179–89. 1980-2015.
[39] Keller C, Tabalaiev K, Marnier G, Noudem J, Sauvage X, Hug E. Influence of spark plasma sintering conditions on the sintering and functional properties of an ultra-fine grained 316L stainless steel obtained from ball-milled powder. Mater Sci Eng, A 2016;665:125–34.
[40] Petrie CM, Sridharan N, Subramanian M, Hehr A, Norfolk M, Sheridan J. Embedded metallized optical fibers for high temperature applications. Smart Mater Struct 2019;28(5):055012.
[41] Marnier G, Keller C, Noudem J, Hug E. Functional properties of a spark plasma sintered ultrafine-grained 316L steel. Mater Des 2014;63:633–40.
[42] Petrie CM, Sridharan N, Hehr A, Norfolk M, Sheridan J. High-temperature strain monitoring of stainless steel using fiber optics embedded in ultrasonically consolidated nickel layers. Smart Mater Struct 2019;28(8):085041.
[43] Dirk H, Jinesh M, William NM, Duncan PH, Robert RJM. Measuring residual stresses in metallic components manufactured with fibre Bragg gratings embedded by selective laser melting. Proc SPIE 2015:96340T.
[44] Okamoto H, Massalski TB, Swartzendruber LJ, Beck PA. The Au−Fe (Gold-Iron) system. Bulletin of Alloy Phase Diagrams 1984;5(6):592–601.
[45] Turchanin MA, Agraval PG, Nikolaenko IV. Thermodynamics of alloys and phase equilibria in the copper-iron system. J Phase Equil 2003;24(4):307–19.
[46] Lupi C, Vendittozzi C, Ciro E, Felli F, Pilone D. Metallurgical aspects of Ni-coating and high temperature treatments for FBG spectrum regeneration. Materials 2023;16(8):2943.
[47] Zhang X, Wang Q, Kane JJ, Rufner JF, Sun C. Graded microstructure and mechanical properties of spark plasma sintered Fe-Cr alloys. J Alloys Compd 2023;967:171448.
[48] Zhang X, McMurtrey MD, Bass RE, Patterson T, Mohale N, Lillo TM, Rufner JF. Enhanced diffusion bonding of alloy 617 using electric field-assisted sintering. J Mater Res Technol 2023;26:7033–51.
[49] Hu Z-Y, Zhang Z-H, Cheng X-W, Wang F-C, Zhang Y-F, Li S-L. A review of multi-physical fields induced phenomena and effects in spark plasma sintering: fundamentals and applications. Mater Des 2020;191:108662.
[50] Farbaniec L, Couque H, Dirras G. Size effects in micro-tensile testing of high purity polycrystalline nickel. Int J Eng Sci 2017;119:192–204.
[51] Ghazanfari A, Li W, Leu MC, Zhuang Y, Huang J. Advanced ceramic components with embedded sapphire optical fiber sensors for high temperature applications. Mater Des 2016;112:197–206.
[52] Kreger S, Froggatt M, Gifford D, Wolfe M, Soller B. Return loss measurement in the presence of variable insertion loss using optical frequency domain reflectometry. A NIST symposium for photonic and fiber measurements. Boulder, Colorado: Optica Publishing Group; 2006CB18.
[53] Mathew J. A method of attaining optical fibre pre-compression for strain and temperature monitoring inside metal at extremely high temperatures. Sensor Actuator Phys 2024;379:116000.